Paternally inherited H3K27me3 affects chromatin accessibility in mouse embryos produced by round spermatid injection

Mizuki Sakamoto[1], Daiyu Ito[1], Rei Inoue[1], Sayaka Wakayama[2], Yasuyuki Kikuchi[1], Li Yang[1], Erika Hayashi[1], Rina Emura[1], Hirosuke Shiura[1], Takashi Kohda[1], Satoshi H. Namekawa[3], Takashi Ishiuchi[1,*], Teruhiko Wakayama[2] and Masatoshi Ooga[1,*,‡]

[1]Faculty of Life and Environmental Sciences, University of Yamanashi, Yamanashi, Japan
[2]Advanced Biotechnology Center, University of Yamanashi, Yamanashi, Japan
[3]Department of Microbiology and Molecular Genetics, University of California Davis, Davis, California, USA

[*]Corresponding authors: tishiuchi@yamanashi.ac.jp (T.I.) and ohga@azabu-u.ac.jp (M.O.)
[‡]Present address: Department of Animal Science and Biotechnology, School of Veterinary Medicine, Azabu University, Kanagawa, Japan. E-mail: ohga@azabu-u.ac.jp

Summary statement: Histone turnover-mediated reduction of H3K27me3 during spermiogenesis is important for chromatin accessibility in early mouse embryos.

Abstract

Round spermatid injection (ROSI) results in a lower birth rate than intracytoplasmic sperm injection, which has hampered its clinical application. Inefficient development of ROSI-embryos has been attributed to epigenetic abnormalities. However, the chromatin-based mechanism that underpins the low birth rate in ROSI remains to be determined. Here, we show that a repressive histone mark H3K27me3 persists from mouse round spermatids into zygotes in ROSI and that round spermatid-derived H3K27me3 is associated with less accessible chromatin and impaired gene expression in ROSI-embryos. These loci are initially marked by H3K27me3 but undergo histone modification remodelling in spermiogenesis, resulting in reduced H3K27me3 in normal spermatozoa. Therefore, the absence of the epigenetic remodelling, presumably mediated by histone turnover during spermiogenesis, leads to dysregulation of chromatin accessibility and transcription in ROSI-embryos. Thus, our results unveil a molecular logic, in which chromatin states in round spermatids impinge on

chromatin accessibility and transcription in ROSI-embryos, highlighting the importance of epigenetic remodelling during spermiogenesis in successful reproduction.

Keywords: zygotic genome activation, chromatin remodelling, round spermatid injection, H3K27me3, epigenetic inheritance, spermiogenesis

Introduction

Round spermatid injection (ROSI) is a valuable and sole method for obtaining offspring from patients with male infertility due to spermatogenesis disruption, especially nonobstructive azoospermia (NOA) (Tekayev and Vuruskan, 2021; Tesarik et al., 1996). Embryos produced by ROSI (ROSI-embryos) can develop to term in mice, rabbits, rats and humans (Hirabayashi et al., 2002; Kimura and Yanagimachi, 1995b; Ogura et al., 1994; Sofikitis et al., 1994; Tesarik et al., 1995). Nevertheless, the success rate of full-term development following ROSI is lower than intracytoplasmic sperm injection (ICSI) embryos. Furthermore, despite reports that healthy offspring were obtained using ROSI in humans, the therapeutic application of ROSI has not been widely adopted due to its uncertain safety (Aslam et al., 1998; Tanaka et al., 2015; Tanaka et al., 2018; Tekayev and Vuruskan, 2021). Therefore, toward its clinical application, it is important to understand at the molecular level why ROSI-embryos show poor development. Current research implies transmitted histone proteins from round spermatid cause abnormalities in the epigenome, transcriptome and, consequently, embryonic development of ROSI-embryos (Hayashi et al., 2003; Kishigami et al., 2006). Ectopic accumulation of a repressive mark H3K9me3 has been found in male pronuclei in 1-cell ROSI-embryos at the pericentromeric heterochromatin regions, suggesting the presence of histone marks inherited from round spermatids (Kishigami et al., 2006). However, the role of paternal chromatin and molecular underpinning of the abnormal transcriptome and poor embryonic development in ROSI-embryos remains to be elucidated.

Male germ cells that reached the haploid round spermatid stage undergo dynamic morphological and physiological changes to form sperm capable of fertilization. This process is known as spermiogenesis and the chromatin structure changes dynamically: histones are replaced by protamine in order to pack the genome into a highly condensed state in sperm (Rathke et al., 2014). Thereby, histone content in sperm is dramatically reduced during spermiogenesis, and accordingly, the distribution of histone modifications and variants, which are tightly linked to gene expression, is dynamically altered (Erkek et al., 2013; Tatehana et al., 2020). Despite the global reduction in histone levels, histones in certain genomic regions are retained in sperm and are considered to be inherited into zygotes (Erkek et al., 2013; Hammoud et al., 2009; Jung et al., 2019; Yamaguchi et al.,

2018; Yoshida et al., 2018). Furthermore, perturbation of an active histone methylation mark (H3K4me3) during spermatogenesis disturbs embryonic development (Lismer et al., 2020; Siklenka et al., 2015), highlighting the importance of inherited epigenome information for embryonic gene expression. In addition to H3K4me3, H3K27me3, a Polycomb repressive complex 2 (PRC2)-mediated repressive mark, is also considered an inheritable epigenetic mark that regulates embryonic gene expression, and H3K4me3 and H3K27me3 together form a bivalent chromatin domain that represents germline developmental potential (Erkek et al., 2013; Lesch et al., 2013; Lesch et al., 2016; Maezawa et al., 2018b; Sin et al., 2015; Teperek et al., 2016). Therefore, the fact that ROSI-embryos receive more histones than ICSI-embryos is likely to be linked to the presence of excessive and undesired histone marks, which may adversely influence the chromatin accessibility landscape and embryonic transcriptome.

We hypothesised that epigenetic information in round spermatids may be transferred to ROSI-embryos, leading to detrimental effects in the regulation of gene expression or chromatin remodelling processes important for embryonic development. Therefore, in this study, we performed a comparative analysis between mouse embryos generated either by ROSI or ICSI using ATAC-seq and RNA-seq. We identified differences in chromatin accessibility as well as gene expression, which were potentially triggered by carried-over epigenetic information. Notably, we found that chromatin regions marked by H3K27me3 in round spermatids but not in mature sperm, are associated with lower accessibility and influence gene expression at zygotic genome activation (ZGA). Therefore, our results demonstrate that spermiogenesis completion is critical for establishing a normal chromatin accessibility landscape as well as for proper embryonic gene expression.

Results

The chromatin accessibility landscape and transcriptome in ROSI- and ICSI-embryos

To investigate the differences in chromatin accessibility and transcriptome between ROSI- and ICSI-embryos, we performed an assay for transposase-accessible chromatin sequencing (ATAC-seq) and RNA-seq for ROSI- and ICSI-embryos at the 1-cell and 2-cell stages (**Fig. 1A**). We selected embryos with two pronuclei (2PN) with normal morphology and 1-cell samples were used after 12–13 hours post-activation or injection (for ROSI or ICSI, respectively) and 28–30 hours for 2-cell samples. In the ATAC-seq, since the number of available embryos upon ROSI and ICSI was limited, we employed Omni ATAC-seq, an improved ATAC-seq protocol (Gou et al., 2020; Ryan Corces et al., 2017). We used 400–450 zygotes and blastomeres per sample with the removal of the 1st and 2nd polar bodies (PB) (**Fig. 1B**). We prepared two biological replicates and obtained at least 21 million reads uniquely mapped to the genome per sample. We also performed RNA-seq. We confirmed that reproducible data were obtained from biological replicates and that our ATAC-seq data for ICSI

2-cell embryos show high similarity with published ATAC-seq data for 2-cell embryos (Wu et al., 2016) (Fig. 1C and Fig. S1A-E). Importantly, in contrast to a previous report, in which ATAC-seq peaks (ATAC peaks) were undetectable at the 1-cell stage (Wu et al., 2016), we detected clear ATAC signals using an improved method.

We first found that ATAC-seq signals in ROSI- and ICSI-embryos show globally similar profiles, suggesting that chromatin remodelling normally occurs in ROSI-embryos (Fig. 1C and D). As expected, ATAC peaks that represent open chromatin regions (Table S1), were observed at active chromatin regions enriched in H3.3 and H3K4me3, but not at H3K27me3-marked repressive chromatin regions in ICSI or ROSI 2-cell embryos (Ishiuchi et al., 2021; Liu et al., 2016; Wang et al., 2018; Wu et al., 2016) (Fig. 1C and D). H3K9me3 was enriched at the transcription start sites (TSSs) associated with relatively high accessibility at the 2-cell stage. This may reflect a non-repressive function of H3K9me3 at these embryonic stages (Burton et al., 2020; Wang et al., 2018). Similar tendencies were also observed in ICSI or ROSI 1-cell embryos, but under a weaker correlation with active marks. This is expected, as H3.3 and H3K4me3 show non-canonical distribution at the 1-cell stage (Ishiuchi et al., 2021; Zhang et al., 2016). For a more detailed analysis of open chromatin regions, we classified gene promoter regions into four clusters by *k*-means clustering based on the strength of ATAC peaks of 1-cell ROSI-, 1-cell ICSI-, 2-cell ROSI- and 2-cell ICSI-embryos. Promoter ATAC signals were positively correlated with gene expression levels. Given the inheritance of maternal mRNA into 1-cell embryos, the positive correlation between gene expression and ATAC-seq signals at the 1-cell stage may indicate that genes actively transcribed in oocytes have high promoter accessibility even at the 1-cell stage (Fig. 1D). Notably, in clusters 1, 2, and 3, we observed gene expression upregulation during development to the 2-cell stage (Fig. S1F), although ATAC signals at their promoters diminished (Fig. 1D). These findings suggest that promoter accessibility correlates with transcriptional output, however, is not the determinant. Therefore, other factors than promoter accessibility may cooperatively fine-tune transcriptional output during ZGA.

Identifying differentially expressed genes in ROSI-embryos

We next investigated how transcriptome is affected in ROSI-embryos. We identified 186 upregulated and 16 downregulated genes in ROSI-embryos at the 1-cell stage [termed as 1-cell ROSI-high and 1-cell ROSI-low differentially expressed genes (DEGs), respectively] (FDR < 0.01, fold change > 1.5) (Fig. 2A, B). At the 1-cell stage, most DEGs were upregulated genes and their gene expression in ICSI-embryos was extremely limited (Fig. 2A and S2A). As the transcription activity at the 1-cell stage is low, we considered that a higher abundance of these transcripts in ROSI 1-cell embryos may reflect carry-over of RNA from round spermatids. To test this hypothesis, we first performed gene ontology (GO) analysis of these genes and identified the terms ‘sperm motility’ and ‘spermatogenesis’ (Fig. 2C). Indeed, transition proteins *Tp1* and *Tp2*, which play a critical role in

spermiogenesis during histone-protamine replacement (Zhao et al., 2004), were contained, which is consistent with a previous study (Hayashi et al., 2003). We then analyzed published RNA-seq data for cells at different spermatogenesis stages to examine their gene expression levels (Hasegawa et al., 2015; Kobayashi et al., 2012). The expression levels of these genes peaked at the round spermatid stage and decreased during maturation into sperm (Fig. 2D). To further investigate this observation, we performed qRT-PCR. For this assay, we prepared 1-cell ROSI-embryos treated with or without DRB that blocks zygotic transcription. Transcripts of 1-cell ROSI-high DEG genes, *Tp1*, *Tp2*, and *Smcp*, showed much higher abundance in ROSI-embryos than ICSI-embryos, and their higher abundance was not affected by DRB treatment (Fig. 2E). In contrast, zygotically expressed genes, such as *Klf5*, were significantly decreased by DRB treatment (Fig. S2B). These results strongly indicate that round spermatid-derived RNA is transferred into ROSI 1-cell embryos.

At the 2-cell stage, when embryos undergo major ZGA, DEGs (649 upregulated and 513 downregulated) were identified in ROSI-embryos (Fig. 2B). We again performed GO analysis and found spermatogenesis-related genes are still enriched in the upregulated gene group in ROSI 2-cell embryos (2-cell ROSI-high DEGs) (Fig. 2C). Accordingly, 54 genes of the 2-cell ROSI-high DEGs overlapped with the 1-cell ROSI-high DEGs (Fig. S2C) and the upregulated status of these 54 genes were maintained between ROSI 1-cell and 2-cell embryos (Fig. S2D). Therefore, RNA carry-over from round spermatids appears to still contribute to differential gene expression at the 2-cell stage. However, its contribution to overall differential expression is small, suggesting ZGA may be affected in ROSI 2-cell embryos. To gain further insight into the mechanisms underlying differential gene expression in ROSI 2-cell embryos, we analysed promoter chromatin accessibility. However, there were no obvious differences in chromatin accessibility at the promoters of DEGs between ICSI- and ROSI-embryos (Fig. 2F), suggesting chromatin accessibility at their promoter is not globally related to the altered transcriptome of ROSI-embryos.

Identifying chromatin regions with differential accessibility in ROSI-embryos

Although ATAC-seq signals were not altered at the DEG promoter regions, we speculated that differential chromatin accessibility outside of these promoters may be associated with abnormal development of ROSI-embryos. We then first performed quantitative analysis of ATAC-seq data (see Material and Methods) and identified ATAC peaks showing higher or lower accessibility in ROSI-embryos compared with ICSI-embryos (referred to as ROSI-high and ROSI-low ATAC peaks, respectively). Although the number of these peaks was limited and more than 90% of total ATAC peaks remained unchanged between ICSI- and ROSI-embryos (classified as common peaks) (Fig. 3A), we further investigated the potential cause of differential chromatin accessibility. The number of ROSI-high peaks was consistently higher than ROSI-low peaks in 1-cell and 2-cell ROSI-embryos, and ROSI-high peaks at the 1-cell stage were frequently observed within the

intronic or intergenic region (Fig. 3B and Fig. S3A). Only a few cases of ROSI-high or low peaks were commonly detected between 1- and 2-cell stages (Fig. S3B). Therefore, most of these differential peaks were developmental stage-specific. Because altered chromatin accessibility upon ROSI application is highly represented in 1-cell ROSI-embryos, we decided to focus on differential chromatin accessibility at the 1-cell stage for further analysis.

To characterize 1-cell ROSI-high and -low ATAC peaks, we analyzed published chromatin immunoprecipitation sequencing (ChIP-seq) data for epigenetic marks in normal embryos (H3.3, H3K4me3, H3K27me3 and H3K9me3) (Ishiuchi et al., 2021; Liu et al., 2016; Wang et al., 2018). 1-cell ROSI-high ATAC peak regions were characterized by weak enrichment of H3K4me3, suggesting that accessible regions are excessively formed in regions where H3K4me3 is not normally enriched (Fig. S3C, D). On the other hand, 1-cell ROSI-low ATAC peak regions were the regions where H3K4me3 but not H3K27me3 is normally enriched. These features were similarly observed at randomly selected ATAC peak regions. Thus, this indicates that 1-cell ROSI-low peak regions display a general feature of accessible regions in normal 1-cell embryos and that accessibility of a small fraction of these H3K4me3-marked and H3K27me3-depleted regions become lower in 1-cell ROSI-embryos. Moreover, enrichment of H3K4me3 at these regions tended to be maintained during early development as well as in ES cells, while H3K27me3 was not enriched (Fig. S3E). Therefore, these results indicate that chromatin accessibility decreased at generally active chromatin regions in 1-cell ROSI-embryos. We then speculated that undesirable inheritance of epigenetic information from round spermatids to ROSI-embryos may result in differential chromatin accessibility. To explore this possibility, we analysed published ATAC-seq and ChIP-seq data for round spermatids and sperm (Erkek et al., 2013; Jung et al., 2019; Maezawa et al., 2018a) (Fig. 3C). We observed higher chromatin accessibility in sperm compared to round spermatids irrespective of 1-cell ROSI-high or 1-cell ROSI-low ATAC peak regions (Fig. 3C and S4A, B). Thus, the differences in chromatin accessibility between round spermatids and sperm did not correlate with differential chromatin accessibility between 1-cell ROSI and ICSI-embryos. Histone H3.3, whose enrichment around the CpG-rich promoters in sperm reflects histone retention (Erkek et al., 2013), was enriched at the 1-cell ROSI-low ATAC peak regions, but not at the 1-cell ROSI-high ATAC peak regions in sperm, suggesting 1-cell ROSI-low ATAC peak regions are the regions where histones are preferentially retained (Fig. 3C). Interestingly, while H3K4me3 enrichment at 1-cell ROSI-high or ROSI-low peak regions was similar between round spermatids and sperm, we observed higher H3K27me3 enrichment in round spermatids compared to sperm at the 1-cell ROSI-low peak regions (Fig. 3C, D and Fig. S4A, B). This observation was confirmed by analyzing other datasets publicly available (Hammoud et al., 2014; Iwamori et al., 2016; Jung et al., 2017) (Fig. S4C). This indicates that H3K27me3-enriched chromatin regions in round spermatids, where its enrichment becomes weaker during maturation into sperm, show lower chromatin

accessibility in 1-cell ROSI-embryos. Notably, this lower chromatin accessibility was cancelled at the 2-cell stage (Fig. 3C and Fig. S3B), thus these changes in accessibility appear to be transient. To explore our hypothesis that H3K27me3 in round spermatids affects the chromatin accessibility in ROSI-embryos, we analyzed the enrichment of H3K27me3 and H3K4me3 at the 1-cell ROSI-high and -low ATAC peak regions as well as at the randomly selected regions in round spermatids. Importantly, we observed significant enrichment of H3K27me3 at the 1-cell ROSI-low ATAC peak regions (Fig. S4D, E). In addition, this region was also mildly enriched in H3K4me3 (Fig. S4D, E). Altogether, these data suggest that chromatin accessibility at regions generally marked by active H3K4me3 in early embryos is suppressed in 1-cell ROSI-embryos possibly due to the inheritance of H3K27me3-marked repressive chromatin states from round spermatids.

To further test our hypothesis that repressive chromatin status is inherited from round spermatids, we performed immunostaining for H3K27me3 at the 1-cell and 2-cell stages. To distinguish paternal and maternal chromatin, we also performed immunostaining for H3K9me2, whose stronger signals were observed on the maternal chromatin at the 1-cell and 2-cell stages (Burton and Torres-Padilla, 2010). Similarly to the previous observation for H3K9me3 (Kishigami et al., 2006), ectopic H3K9me2 signals were observed at the pericentromeric heterochromatin region in male PN of ROSI 1-cell embryos (Fig. 4A, B). On the contrary, at the 1-cell stage, H3K27me3 intensity in male pronuclei in ROSI-embryos was globally higher than that in ICSI-embryos (Fig. 4A, B). Furthermore, consistent with this observation, asymmetric H3K27me3 signals between parental chromosomes in ICSI 2-cell embryos was not observed in ROSI 2-cell embryos (Fig. 4C). Round spermatids showed higher signals for H3K27me3, but not sperm (Fig. 4D), suggesting ROSI-embryos may possess an abnormal landscape of H3K27me3 by inheriting this mark from round spermatids. We also asked whether there are any other histone marks that would alter chromatin accessibility in ROSI-embryos. Among the histone marks analyzed (H3K4me1, H3K4me3, H3K27me3, and H3K36me3), remodelling of H3K4me1 during spermiogenesis was also observed, but this modification was similarly enriched in both 1-cell ROSI-high and low ATAC peak regions (Fig. S4C). Thus, at this point, H3K27me3 is the only histone mark tightly associated with altered chromatin accessibility in ROSI-embryos.

Altered chromatin accessibility in ROSI-embryos affects transcription

H3K27me3 represses gene expression (reviewed in Zhang et al., 2015). Therefore, we next investigated whether lower chromatin accessibility in ROSI 1-cell embryos is associated with changes in gene expression. We classified ATAC peaks into distal ATAC peaks and promoter ATAC peaks (peaks at TSS ± 1 kb). We observed no changes in gene expression when focused on distal ATAC peaks or ROSI-high ATAC peaks (Fig. 5A). In contrast, gene expression associated with ROSI-low promoter ATAC peaks (146 genes) was lower than ICSI-embryos (Fig. 5A and S5A-D).

Lower expression was prominent at the 2-cell stage, which suggests that promoter chromatin accessibility at the 1-cell stage might be important for future gene activation. Furthermore, we found that the 1-cell ROSI-low promoter ATAC peaks that show H3K27me3 enrichment in round spermatids (H3K27me3 RPKM > 1 in round spermatid) are mainly associated with this lower gene expression (Fig. S6A). Notably, while the tendency of downregulation was observed in this gene group, only a few DEGs (FDR < 0.01 and FC >1.5 as seen in Fig. 2B) were included (Fig. 5B), indicating that lower chromatin accessibility only mildly affects transcription.

Our immunostaining data revealed that the distribution of H3K27me3 in ROSI-embryos differed largely from ICSI-embryos, and therefore we hypothesised that inheritance of H3K27me3 from round spermatids may suppress gene expression without altering chromatin accessibility. We then analyzed H3K27me3 and H3K4me3 enrichment in round spermatids or sperm around the TSSs of DEGs at the 2-cell stage. Interestingly, prominent enrichment of H3K27me3 as well as mild enrichment of H3K4me3 was observed at the ROSI-low DEG promoters in round spermatids, but H3K27me3 enrichment diminished in sperm (Fig. 5C, D and S6B). In contrast, weaker H3K27me3 enrichment as well as higher enrichment of H3K4me3 was observed at the ROSI-high DEG promoters in round spermatids, indicating that the promoters of 2-cell high and low DEGs possess bivalent H3K4me3 and H3K27me3 modifications at different levels in round spermatids. Given the previous observation that bivalent promoters in round spermatids are prevalent for genes expressed after fertilization (Lesch et al., 2013; Lesch et al., 2016; Maezawa et al., 2018b; Sin et al., 2015), our results suggest that removal of H3K27me3 during spermiogenesis might be prerequisite for proper embryonic transcription.

Identification of transcription factor motifs at the chromatin regions with differential accessibility

The results above indicated that the inheritance of repressive chromatin status from round spermatids might cause lower chromatin accessibility and altered gene expression in ROSI-embryos. However, we did not find any possible involvement of histone modifications in acquisition of higher chromatin accessibility in ROSI-embryos (Fig. 3C and Fig. S4C). Thereby, we suspected that an alternative mechanism such as a transcription factor (TF)-driven mechanism might be involved in this process. To explore this possibility, we performed a TF motif analysis on 1-cell ROSI-high, ROSI-low, and ROSI-common ATAC peaks. We obtained some TF motifs at these peaks (Fig. S7A). Among the identified motifs, we focused on SOX30, a member of the SOX TF family, as it was highly expressed in spermatocytes and round spermatids and the SOX30 motif was uniquely identified at the 1-cell ROSI-high ATAC peaks (Bai et al., 2018; Osaki et al., 1999; Zhang et al., 2018) (Fig. S7B). To examine whether SOX30 was enriched at 1-cell ROSI-high ATAC peak regions in round spermatids, we analyzed published SOX30 ChIP-seq data in round spermatids (Chen et al., 2018a).

However, the enrichment of SOX30 was weak in these regions (Fig. S7C). Nevertheless, we consider that it would be possible that SOX30 carried over from round spermatids binds to genomic regions where SOX30 did not bind in round spermatids as large-scale chromatin remodelling occurs in early embryos. Next, we attempted to perform immunostaining for SOX30 at the 1-cell stage. However, we were not able to detect reliable SOX30 signals in ROSI-embryos (data not shown). Although we could not identify factors which contribute to the higher chromatin accessibility in ROSI-embryos, it would be important to identify RNAs or proteins transmitted from round spermatids in future studies to comprehensively understand the chromatin alteration in ROSI-embryos.

Discussion

To our best knowledge, this is the first report identifying the relationship between altered transcriptome and chromatin accessibility in ROSI-embryos. Our transcriptome analysis revealed that ROSI-embryos have RNA transmitted from round spermatids, as suggested previously (Hayashi et al., 2003). The number of detected DEGs was limited at the 1-cell stage, which is consistent with limited zygotic transcriptional activity during this stage. In contrast, we detected a larger number of DEGs at the 2-cell stage, possibly due to a transcriptional burst, called major ZGA, during this stage. Conversely, we found the number of differential accessible regions decreased during transition from 1- to 2-cell stages (Fig. 3B). Therefore, while defects in chromatin accessibility are corrected to some extent during development, ROSI-embryos are likely to suffer from altered gene expression. However, we cannot exclude the possibility that there may be more defects in transcription in 1-cell ROSI-embryos than detected in this study as it is hard to see a relatively low amount of zygotic transcripts with a conventional RNA-seq at this stage.

By focusing on differentially accessible chromatin regions, we found that lower accessible regions in 1-cell ROSI-embryos are marked by H3K27me3 in round spermatids. Supporting this observation, we detected the presence of ectopic H3K27me3 in ROSI-embryos. This finding prompted us to observe genes significantly downregulated in ROSI-embryos were associated with high levels of H3K27me3 in round spermatids. Therefore, we propose transmission of H3K27me3 from round spermatids lowers chromatin accessibility at the 1-cell stage and alters gene expression profiles at the 2-cell stage in ROSI-embryos (Fig. 6). This lower accessibility appeared to be corrected at the 2-cell stage (Fig. 3C and S4B). These data suggest that chromatin accessibility at the 1-cell stage is important to regulate gene expression at the 2-cell stage although there is still a possibility that ectopic H3K27me3 directly influences gene expression without altering chromatin accessibility at the 2-cell stage. We also noticed that lower accessible regions in 1-cell ROSI-embryos showed high enrichment of H3.3 in sperm, but not in round spermatids. During spermiogenesis, histone H3 variant H3T is typically replaced by H3.3, another histone variant (Ueda et al., 2017). Therefore,

H3K27me3 is likely to be inherited into ROSI-embryos under the absence of this process. Thus, our results highlight the biological significance of chromatin remodelling during spermiogenesis for fine-tuning gene expression after fertilization.

In sperm, H3K27me3 at the 1-cell ROSI-low ATAC peak regions decreased, but H3K4me3 was still enriched. Therefore, fertilized embryos inheriting H3.3 marked by H3K4me3 may be advantageous for embryonic gene activation (Fig. 6). These observations imply manipulating H3K27me3 inheritance may help improve low birth rates of ROSI-embryos. Recently, a study reported that treating round spermatids with TSA before round spermatids were injected into oocytes improved the development of ROSI-embryos to the blastocyst stage (Hosseini and Salehi, 2021). Although exploring whether TSA treatment improves their full-term development is still essential, this method may be useful for identifying potential causes of low birth rates of ROSI-embryos. Because previous studies reported that global levels of H3K27me3 decreased following TSA treatment in somatic cell nuclear transfer derived embryos and ES cells (Karantzali et al., 2008; Selokar et al., 2016), it is possible that improved development of ROSI-embryos by TSA is due to reduced H3K27me3 levels in round spermatid. Therefore, identifying the genomic distribution of H3K27me3 in ROSI-derived embryos in an allele-discriminative manner would be crucial given the recent progress in low-input epigenetic analytical techniques. These analyses will clearly pinpoint comprehensive knowledge on not only the causes of low birth rates but also the epigenetic events during spermiogenesis essential for embryonic development.

Materials and Methods

Animals and oocyte collection and culture

We used 8 to 12-week-old female ICR (for ATAC-seq; n = 247) and C57BL/6 (for RNA-seq; n = 72) mice as oocyte donors. Same strain male mice (ICR: n = 12, C57BL/6: n = 9) were also used as the sperm donor. All animal experiments were approved by the Ethics Committee of the University of Yamanashi (reference number: A29-24) and conducted following Guide for the Care and Use of Laboratory Animals and ARRIVE guidelines. All mice were housed under specific pathogen-free conditions at a constant temperature of 25ºC, relative humidity of 50% and a 14/10-h light/dark period with *ad libitum* access to a commercial diet and distilled water. In this study, body weight was not measured because the body weight of young mice does not affect embryo quality.

ROSI and ICSI

Cumulus cell and oocyte complexes (COCs) were obtained from super-ovulated ICR and C57BL/6 female mice by injection of 7.5 IU equine chorionic gonadotropin (ASKA Pharmaceutical CO., Ltd., Tokyo, Japan) and human chorionic gonadotropin (ASKA Pharmaceutical) at 46–50 h intervals. Obtained COCs were treated with hyaluronidase for 10 min in HEPES-buffered CZB medium

(CZB-HEPES) (Kimura and Yanagimachi, 1995a). For ICSI, sperm were collected from the cauda epididymis, then cultured in human tubal fluid (Quinn et al., 1995) for capacitation for 1 h. Before cytosolic injection of denuded oocytes, sperm tails were eliminated with a Piezo drive micromanipulator (Prime Tech Ltd., Ibaraki, Japan) in CZB-HEPES medium supplemented with 10% PVP (10% PVP-CZB-HEPES). After cutting the tail, the zona pellucida and cytosolic membranes were also disrupted with a Piezo drive micromanipulator. For ROSI, the obtained testes were minced with scissors, sieved through a Mini Cell Strainer and then re-suspended in 10% PVP-CZB-HEPES. The nucleus of each round spermatid was collected with a narrow pipette (7–8 μm diameter). The zona pellucida and cytosolic membrane were disrupted as per the ICSI. The oocytes injected with round spermatid nuclei were activated by culturing in Ca^{2+}-free CZB medium containing 5 mM $SrCl_2$ for 1–2 h.

Removal of PB

Zygotes were treated with cytochalasin B (CB) before elimination for 10–20 min in KSOM, then moved to CB containing CZB-HEPES. The zona pellucida was broken by a Piezo drive micromanipulator. We then vacuumed the 2nd PB with a pipette (10 μm diameter, **Fig. 1B**). The zona pellucida was solved by Acidic Tyrode. During the wash, the 1st PB was eliminated by repeated pipetting. Embryos were then cultured in KSOM until sample collection.

Omni-assay for transposase accessibility chromatin sequence (Omni-ATAC-seq)

We collected 411–450 zygotes and 210–231 2-cell stage ICR embryos (corresponds to 420–462 blastomeres, respectively) for each sample. We then performed omni-ATAC following methods of a previous study (Ryan Corces et al., 2017) with small modifications. To avoid embryo loss, we collected live embryos without PB and zona pellucida were transferred into cold ATAC-resuspension buffer and mixed by tapping. After ATAC-reaction for 30 min at 37ºC, DNA products were cleaned with a MinElute PCR purification kit (Qiagen). We stored 22 ul of the eluted samples at −20ºC until subsequent PCR amplification. After 5 cycles of pre-amplification, we performed an additional PCR for 9 cycles. Amplified DNA was purified by a MinElute PCR purification kit. The amplified ATAC-seq libraries were subjected to sequencing by Novaseq 6000 (150-nt paired-end sequencing).

RNA-seq

RNA was extracted from 50 zygotes and 49–96 2-cell stage embryos (C57BL/6 background) with ISOGEN II (NIPPON GENE, Tokyo, Japan), according to the manufacturer's instructions. We performed RNA quality analysis on the Bioanalyzer RNA Pico Chip (Agilent Technologies Santa Clara, Ca, USA). RNA-seq libraries were constructed by SMART-seq stranded kit with 1 ng of extracted total RNA according to the manufacturer's instructions. RNA fragmentation was then

conducted for 2 min. To amplify constructed cDNA, we performed PCR1 (94ºC for 1 min, 5 cycles of 98ºC for 15 sec, 55ºC for 15 sec, 68ºC for 30 sec and 68ºC for 2 min) and PCR2 (94ºC for 1 min, 14 cycles of 98ºC for 15 sec, 55ºC for 15 sec and 68ºC for 30 sec). The amplified RNA-seq libraries were then subjected to sequencing using Novaseq 6000 (100-nt paired-end sequencing).

Immunostaining

ICSI and ROSI-derived-zygotes and 2-cell stage embryos were collected at 10 and 28–30 hpi or hpa, respectively. Embryos were fixed by 4% paraformaldehyde (PFA) containing 0.2% Triton X-100 (Tx) in PBS, then washed in PBS containing 1% BSA and 0.2% Tween (Tw, 1% BSA–0.2% Tw). H3K27me3 rabbit polyclonal antibody (Millipore 07–449, 1:500; Validation data: https://www.merckmillipore.com/JP/ja/product/Anti-trimethyl-Histone-H3-Lys27-Antibody,MM_NF-07-449), H3K9me2 mouse monoclonal antibody (Abcam ab1220, 1:500; Validation data: https://www.abcam.co.jp/histone-h3-di-methyl-k9-antibody-mabcam-1220-chip-grade-ab1220.html) and the embryos were incubated with at 4ºC overnight. Embryos were then washed by 1% BSA–0.2% Tw and incubated with a second antibody against rabbit IgG labelled with Alexa flour 488 or 568 (Invitrogen A11034 or A11011, 1:500). The immune-stained embryos were then mounted on an antifade mounting medium with DAPI (4',6-diamidino-2-phenilindole, Vector Laboratories, Burlingame, CA). Fluorescence signals were detected using confocal microscopes FV1000 or FV1200 (Olympus Corporation, Tokyo, Japan). For quantitative analysis of H3K27me3 levels, we measured fluorescence signal intensity using ImageJ software (Schindelin et al., 2012). We then divided the H3K27me3 signal in each nucleus using the DAPI signal for normalisation. Statistical analysis was performed using Prism 9 software (Graph pad, Inc., San Diego, CA, USA). Sperm and round spermatids obtained from minced seminiferous tubules were mounted on slides and fixed in 4% PFA containing 0.2% Tx in PBS for 20 min. Specimens were washed in PBS containing 1% BSA and immunostained for H3K27me3. The H3K27me3 signal in sperm and round spermatids was detected using confocal microscopes FV1200 (Olympus Corporation, Tokyo, Japan).

Treatment with DRB and quantitative real-time polymerase chain reaction (qRT-PCR)

Ten ICSI or ROSI 1-cell embryos at 10 hpi or hpa were pooled per sample. To inhibit transcription in ROSI-embryos, MII oocytes were cultured in KSOM containing 80 µM DRB (Sigma-Aldrich) before ROSI, and ROSI-embryos were then cultured in the presence of DRB.

The samples were added with 5,000 copies of H2B-eGFP mRNA (Ooga et al., 2016) as an external control. Quantitative real-time polymerase chain reaction (PCR) was performed using a CellAmp Direct RNA Prep Kit (TAKARA) and One Step TB Green PrimeScript RT-PCR Kit II (TAKARA) following the manufacturer's instructions. After treatment with DNase I to remove genomic DNA, cell lysates containing total RNA were used as a template for a 10 µl qRT-PCR reaction. The primers

used were as follows: Tp1 (5′- GAGGAGAGGCAAGAACCGAG and 5′- CGGTAATTGCGACTTGCATCA); Tp2 (5′-GCACTCTCGACACTCACCTG and 5′- TGTATCTTCGCCCTGAGCTA); Smcp (5′- GTTGCCAGATCAGGAACTCCA and 5′- TGGACAGCACGGTTTAGGTG); eGFP (5′- GCTACCCCGACCACATGAAG and 5′- TCTTGTAGTTGCCGTCGTCC); Duxf3 (5′- CCTCAAAGAGGTCCATCAGAGG and 5′-TGAAACCATATGTGGATCGTGTC); MERVL (5′- CTCTACCACTTGGACCATATGAC and 5′- GAGGCTCCAAACAGCATCTCTA); Nid2 (5′- CACCGAGGACAGTTTCCATT and 5′- CCAGTTACCAGGTGCTGGAT); Klf5 (5′- ACGTACACCATGCCAAGTCA and 5′- GTGGGAGAGTTGGCGAATTA) (Abe et al., 2018).

ATAC-seq data processing

Adaptor and low-quality sequences were removed by *fastp* (version 0.20.1) (Chen et al., 2018b) with option '-l 30 -w 10'. Reads were aligned to the mouse genome (mm10) using Bowtie2 (version 2.4.3) (Langmead and Salzberg, 2012) with option '--no-mixed --no-discordant -X 2000' and unmapped reads were discarded by Samtools (version 1.4.1) (Li et al., 2009) with option '-F 0x4'. Reads from PCR duplicates were removed using Picard MarkDuplicates (version 2.23.8) (https://broadinstitute.github.io/picard/). For suiting similar read numbers between replications, reads were divided using 'divide_bam.py' in RseQC (Wang et al., 2012). After confirming reproducibility between replicates, they were merged using Samtools 'merge'. To identify differentially accessible chromatin regions and common peak regions between ROSI and ICSI-embryos, each replication peak was first called by MACS2 (version 2.2.7.1) (Zhang et al., 2008) with the option '--nomodel --shift -90 --extsize 180 -f BAMPE -B -q 0.01 -g mm'. Overlapping regions from each replication were then calculated using BEDtools (Quinlan and Hall, 2010) intersect. Overlapping regions and merged read data were used to calculate normalised read density between samples using MAnorm (version 1.3.0) (Shao et al., 2012) and identify differentially accessible chromatin regions under the conditions of fold change > 1.5 (M-value in MAnorm output data). Published ATAC-seq data (GSE102954, GSE116854, GSE66390) (Jung et al., 2019; Maezawa et al., 2018a; Wu et al., 2016) were also processed similarly and aligned to the mouse genome, as described above. *K*-means clustering and heatmap depiction were conducted by *computeMatrix* and *plotHeatmap* in deepTools (version 3.5.1) (Ramírez et al., 2016). ATAC peaks were annotated with nearby genes using annotatePeaks.pl (used GENCODE vM12 database) from HOMER (Heinz et al., 2010) and defined at least ± 1.0 kb away from the TSS as distal peaks. findMotifsGenome.pl from HOMER program with default option was used for finding the sequence motif enriched in ATAC-seq peaks.

RNA-seq data processing

Adaptor and low-quality sequences were removed by *fastp* with the option '-l 50 -w 10'. Reads corresponding to ribosomal RNA were discarded from analysis by extracting reads unmapped to ribosomal DNA using Bowtie2. Subsequently, reads were aligned to the mouse genome (mm10) using STAR (version 2.7.4a) (Dobin et al., 2013). Read counts were calculated by featureCounts (Rsubread version 2.4.3 package in R) (Liao et al., 2014; Liao et al., 2019). To identify DEGs between ROSI and ICSI-embryos, the read count data were processed by EdgeR (version 3.32.1) (Robinson et al., 2010). Genes with false discovery rate (FDR) < 0.01 and fold change > 1.5 or < 0.67 were used to identify DEGs. We then performed GO enrichment analyses using DAVID (Huang et al., 2009a; Huang et al., 2009b). Published RNA-seq data (GSE55060 and DRA000484, E-MTAB-2950) (Abe et al., 2015; Hasegawa et al., 2015; Kobayashi et al., 2012) were also processed, as described above. Transcripts per million (TPM) of each gene annotated by GENCODE vM12 was quantified with R (http://www.r-project.org/). The *cor* and *hclust* functions with option 'method = ward.D2' in R were used to calculate Spearman rank correlation coefficient and perform hierarchical clustering, respectively. We performed principal component analysis using the *prcomp* function in R and *ggplot* (package ggplot2 version 3.3.5) was used for plotting. We performed *k*-means clustering after calculating z-scores based on TPM values and heatmaps using the *pheatmap.type* function (package Pigengene version 1.16.0). Kruskal–Wallis test (**Fig. 5A**) was performed using the R package *ggpubr* version 0.4.0.

ChIP-seq data processing

Published ChIP-seq data were obtained from GSE139527, GSE73952, GSE97778 GSE42629 GSE49624 GSE79230, DRA004778 and GSE107644 (Chen et al., 2018a; Erkek et al., 2013; Hammoud et al., 2014; Ishiuchi et al., 2021; Iwamori et al., 2016; Jung et al., 2017; Liu et al., 2016; Wang et al., 2018). Reads were aligned to the mouse genome (mm10) using Bowtie2 with the option '--no-mixed --no-discordant' after removing adaptor and low-quality sequences using *fastp*. Unmapped reads were removed using Samtools with option '-F 0x4' and PCR duplicates were removed using Picard MarkDuplicates. Heatmaps were plotted using *computeMatrix* and *plotHeatmap* in deepTools. The average read tag density at the promoter region of each DEG group was analysed by ngs.plot.r (version 2.47.1) (Shen et al., 2014).

Quantification and Statistical Analysis

Statistical analyses were implemented with R or Prism 9 (GraphPad Software, Inc., San Diego, CA, USA). Data for two experimental groups were analyzed using a two-tailed Wilcoxon rank-sum test.

Acknowledgements

We thank Drs. Satoshi Kamimura, Jafar Sharif, So Maezawa, Akihiko Sakashita, Satoshi Kishigami, Mr. Kousuke Kazama, Miss Mayu Tatara and members of T.W. laboratory and University of Yamanashi, Advanced Biotechnology Centre for constructive discussions and technical assistance with the NGS analysis. This work was supported by JSPS KAKENHI grant number 16H06279 (PAGS).

Competing interests

The authors have no competing interests to declare.

Funding

Financial support for this research was provided by a Grant-in-Aid for Young Scientists (grant no. 19K16012) to M.O., a MEXT Grant-in-Aid for Scientific Research on Innovative Areas to T.I. (grant no. JP19H05756) and the Asada Science Foundation and the Canon Foundation (grant no. M20-0006) to T.W.

Author contributions

Conceptualization: T.W. and M.O.; Sample preparation: D.I., R.I., S.W., Y.K., Y.L. E.H., R.E., H.S., T.W., M.O.; Data analysis. M.S., S.W., T.K., S.H.N., T.I., T.W., M.O.; Writing: M.S., S.H.N., T.I., M.O.

Data availability

Sequence data reported in this paper are available on the DDBJ: DRA010218, DRA011368, DRA010219 and DRA011577. Alternatively, all data are also deposited to GEO with the accession number GSE196859.

References

Abe, K.-I., Yamamoto, R., Franke, V., Cao, M., Suzuki, Y., Suzuki, M. G., Vlahovicek, K., Svoboda, P., Schultz, R. M. and Aoki, F. (2015). The first murine zygotic transcription is promiscuous and uncoupled from splicing and 3' processing. *EMBO J.* **34**, 1523–1537.

Abe, K.-I., Funaya, S., Tsukioka, D., Kawamura, M., Suzuki, Y., Suzuki, M. G., Schultz, R. M. and Aoki, F. (2018). Minor zygotic gene activation is essential for mouse preimplantation development. *Proc. Natl. Acad. Sci. U. S. A.* **115**, E6780–E6788.

Aslam, I., Fishel, S., Green, S., Campbell, A., Garratt, L., McDermott, H., Dowell, K. and Thornton, S. (1998). Can we justify spermatid microinjection for severe male factor infertility? *Hum. Reprod. Update* **4**, 213–222.

Bai, S., Fu, K., Yin, H., Cui, Y., Yue, Q., Li, W., Cheng, L., Tan, H., Liu, X., Guo, Y., et al. (2018). Sox30 initiates transcription of haploid genes during late meiosis and spermiogenesis in mouse testes. *Development* **145**,.

Burton, A. and Torres-Padilla, M.-E. (2010). Epigenetic reprogramming and development: a unique heterochromatin organization in the preimplantation mouse embryo. *Brief. Funct. Genomics* **9**, 444–454.

Burton, A., Brochard, V., Galan, C., Ruiz-Morales, E. R., Rovira, Q., Rodriguez-Terrones, D., Kruse, K., Le Gras, S., Udayakumar, V. S., Chin, H. G., et al. (2020). Heterochromatin establishment during early mammalian development is regulated by pericentromeric RNA and characterized by non-repressive H3K9me3. *Nat. Cell Biol.* **22**, 767–778.

Chen, Y., Zheng, Y., Gao, Y., Lin, Z., Yang, S., Wang, T., Wang, Q., Xie, N., Hua, R., Liu, M., et al. (2018a). Single-cell RNA-seq uncovers dynamic processes and critical regulators in mouse spermatogenesis. *Cell Res.* **28**, 879–896.

Chen, S., Zhou, Y., Chen, Y. and Gu, J. (2018b). fastp: an ultra-fast all-in-one FASTQ preprocessor. *Bioinformatics* **34**, i884–i890.

Dobin, A., Davis, C. A., Schlesinger, F., Drenkow, J., Zaleski, C., Jha, S., Batut, P., Chaisson, M. and Gingeras, T. R. (2013). STAR: ultrafast universal RNA-seq aligner. *Bioinformatics* **29**, 15–21.

Erkek, S., Hisano, M., Liang, C.-Y., Gill, M., Murr, R., Dieker, J., Schübeler, D., Vlag, J. van der, Stadler, M. B. and Peters, A. H. F. M. (2013). Molecular determinants of nucleosome retention at CpG-rich sequences in mouse spermatozoa. *Nat. Struct. Mol. Biol.* **20**, 868–875.

Gou, L.-T., Lim, D.-H., Ma, W., Aubol, B. E., Hao, Y., Wang, X., Zhao, J., Liang, Z., Shao, C., Zhang, X., et al. (2020). Initiation of Parental Genome Reprogramming in Fertilized Oocyte by Splicing Kinase SRPK1-Catalyzed Protamine Phosphorylation. *Cell* **180**, 1212-1227.e14.

Hammoud, S. S., Nix, D. A., Zhang, H., Purwar, J., Carrell, D. T. and Cairns, B. R. (2009). Distinctive chromatin in human sperm packages genes for embryo development. *Nature* **460**, 473–478.

Hammoud, S. S., Low, D. H. P., Yi, C., Carrell, D. T., Guccione, E. and Cairns, B. R. (2014). Chromatin and transcription transitions of mammalian adult germline stem cells and spermatogenesis. *Cell Stem Cell* **15**, 239–253.

Hasegawa, K., Sin, H.-S., Maezawa, S., Broering, T. J., Kartashov, A. V., Alavattam, K. G., Ichijima, Y., Zhang, F., Bacon, W. C., Greis, K. D., et al. (2015). SCML2 establishes the male germline epigenome through regulation of histone H2A ubiquitination. *Dev. Cell* **32**, 574–588.

Hayashi, S., Yang, J., Christenson, L., Yanagimachi, R. and Hecht, N. B. (2003). Mouse preimplantation embryos developed from oocytes injected with round spermatids or spermatozoa have similar but distinct patterns of early messenger RNA expression. *Biol. Reprod.* **69**, 1170–1176.

Heinz, S., Benner, C., Spann, N., Bertolino, E., Lin, Y. C., Laslo, P., Cheng, J. X., Murre, C., Singh, H. and Glass, C. K. (2010). Simple combinations of lineage-determining transcription factors prime cis-regulatory elements required for macrophage and B cell identities. *Mol. Cell* **38**, 576–589.

Hirabayashi, M., Kato, M., Aoto, T., Ueda, M. and Hochi, S. (2002). Rescue of infertile transgenic rat lines by intracytoplasmic injection of cryopreserved round spermatids. *Mol. Reprod. Dev.* **62**, 295–299.

Hosseini, S. and Salehi, M. (2021). Tricostatin A-treated round spermatid enhances preimplantation embryo developmental competency following round spermatid injection in mice. *Zygote* 1–7.

Huang, D. W., Sherman, B. T. and Lempicki, R. A. (2009a). Systematic and integrative analysis of large gene lists using DAVID bioinformatics resources. *Nat. Protoc.* **4**, 44–57.

Huang, D. W., Sherman, B. T. and Lempicki, R. A. (2009b). Bioinformatics enrichment tools: paths toward the comprehensive functional analysis of large gene lists. *Nucleic Acids Res.* **37**, 1–13.

Ishiuchi, T., Abe, S., Inoue, K., Yeung, W. K. A., Miki, Y., Ogura, A. and Sasaki, H. (2021). Reprogramming of the histone H3.3 landscape in the early mouse embryo. *Nat. Struct. Mol. Biol.* **28**, 38–49.

Iwamori, N., Tominaga, K., Sato, T., Riehle, K., Iwamori, T., Ohkawa, Y., Coarfa, C., Ono, E. and Matzuk, M. M. (2016). MRG15 is required for pre-mRNA splicing and spermatogenesis. *Proc. Natl. Acad. Sci. U. S. A.* **113**, E5408-15.

Jung, Y. H., Sauria, M. E. G., Lyu, X., Cheema, M. S., Ausio, J., Taylor, J. and Corces, V. G. (2017). Chromatin States in Mouse Sperm Correlate with Embryonic and Adult Regulatory Landscapes. *Cell Rep.* **18**, 1366–1382.

Jung, Y. H., Kremsky, I., Gold, H. B., Rowley, M. J., Punyawai, K., Buonanotte, A., Lyu, X., Bixler, B. J., Chan, A. W. S. and Corces, V. G. (2019). Maintenance of CTCF- and Transcription Factor-Mediated Interactions from the Gametes to the Early Mouse Embryo. *Mol. Cell* **75**, 154-171.e5.

Karantzali, E., Schulz, H., Hummel, O., Hubner, N., Hatzopoulos, A. and Kretsovali, A. (2008). Histone deacetylase inhibition accelerates the early events of stem cell differentiation: transcriptomic and epigenetic analysis. *Genome Biol.* **9**, R65.

Kimura, Y. and Yanagimachi, R. (1995a). Intracytoplasmic sperm injection in the mouse. *Biol. Reprod.* **52**, 709–720.

Kimura, Y. and Yanagimachi, R. (1995b). Mouse oocytes injected with testicular spermatozoa or round spermatids can develop into normal offspring. *Development* **121**, 2397–2405.

Kishigami, S., Van Thuan, N., Hikichi, T., Ohta, H., Wakayama, S., Mizutani, E. and Wakayama, T. (2006). Epigenetic abnormalities of the mouse paternal zygotic genome associated with microinsemination of round spermatids. *Dev. Biol.* **289**, 195–205.

Kobayashi, H., Sakurai, T., Imai, M., Takahashi, N., Fukuda, A., Yayoi, O., Sato, S., Nakabayashi, K., Hata, K., Sotomaru, Y., et al. (2012). Contribution of intragenic DNA methylation in mouse gametic DNA methylomes to establish oocyte-specific heritable marks. *PLoS Genet.* **8**, e1002440.

Langmead, B. and Salzberg, S. L. (2012). Fast gapped-read alignment with Bowtie 2. *Nat. Methods* **9**, 357–359.

Lesch, B. J., Dokshin, G. A., Young, R. A., McCarrey, J. R. and Page, D. C. (2013). A set of genes critical to development is epigenetically poised in mouse germ cells from fetal stages through completion of meiosis. *Proc. Natl. Acad. Sci. U. S. A.* **110**, 16061–16066.

Lesch, B. J., Silber, S. J., McCarrey, J. R. and Page, D. C. (2016). Parallel evolution of male germline epigenetic poising and somatic development in animals. *Nat. Genet.* **48**, 888–894.

Li, H., Handsaker, B., Wysoker, A., Fennell, T., Ruan, J., Homer, N., Marth, G., Abecasis, G., Durbin, R. and 1000 Genome Project Data Processing Subgroup (2009). The Sequence Alignment/Map format and SAMtools. *Bioinformatics* **25**, 2078–2079.

Liao, Y., Smyth, G. K. and Shi, W. (2014). featureCounts: an efficient general purpose program for assigning sequence reads to genomic features. *Bioinformatics* **30**, 923–930.

Liao, Y., Smyth, G. K. and Shi, W. (2019). The R package Rsubread is easier, faster, cheaper and better for alignment and quantification of RNA sequencing reads. *Nucleic Acids Res.* **47**, e47.

Lismer, A., Siklenka, K., Lafleur, C., Dumeaux, V. and Kimmins, S. (2020). Sperm histone H3 lysine 4 trimethylation is altered in a genetic mouse model of transgenerational epigenetic inheritance. *Nucleic Acids Res.* **48**, 11380–11393.

Liu, X., Wang, C., Liu, W., Li, J., Li, C., Kou, X., Chen, J., Zhao, Y., Gao, H., Wang, H., et al. (2016). Distinct features of H3K4me3 and H3K27me3 chromatin domains in pre-implantation embryos. *Nature* **537**, 558–562.

Maezawa, S., Yukawa, M., Alavattam, K. G., Barski, A. and Namekawa, S. H. (2018a). Dynamic reorganization of open chromatin underlies diverse transcriptomes during spermatogenesis. *Nucleic Acids Res.* **46**, 593–608.

Maezawa, S., Hasegawa, K., Yukawa, M., Kubo, N., Sakashita, A., Alavattam, K. G., Sin, H.-S., Kartashov, A. V., Sasaki, H., Barski, A., et al. (2018b). Polycomb protein SCML2 facilitates H3K27me3 to establish bivalent domains in the male germline. *Proc. Natl. Acad. Sci. U. S. A.* **115**, 4957–4962.

Majumder, S., Miranda, M. and DePamphilis, M. L. (1993). Analysis of gene expression in mouse preimplantation embryos demonstrates that the primary role of enhancers is to relieve repression of promoters. *EMBO J.* **12**, 1131–1140.

Ogura, A., Matsuda, J. and Yanagimachi, R. (1994). Birth of normal young after electrofusion of mouse oocytes with round spermatids. *Proc. Natl. Acad. Sci. U. S. A.* **91**, 7460–7462.

Ooga, M., Fulka, H., Hashimoto, S., Suzuki, M. G. and Aoki, F. (2016). Analysis of chromatin structure in mouse preimplantation embryos by fluorescent recovery after photobleaching. *Epigenetics* **11**, 85–94.

Osaki, E., Nishina, Y., Inazawa, J., Copeland, N. G., Gilbert, D. J., Jenkins, N. A., Ohsugi, M., Tezuka, T., Yoshida, M. and Semba, K. (1999). Identification of a novel Sry-related gene and its germ cell-specific expression. *Nucleic Acids Res.* **27**, 2503–2510.

Quinlan, A. R. and Hall, I. M. (2010). BEDTools: a flexible suite of utilities for comparing genomic features. *Bioinformatics* **26**, 841–842.

Quinn, P., Moinipanah, R., Steinberg, J. M. and Weathersbee, P. S. (1995). Successful human in vitro fertilization using a modified human tubal fluid medium lacking glucose and phosphate ions. *Fertil. Steril.* **63**, 922–924.

Ramírez, F., Ryan, D. P., Grüning, B., Bhardwaj, V., Kilpert, F., Richter, A. S., Heyne, S., Dündar, F. and Manke, T. (2016). deepTools2: a next generation web server for deep-sequencing data analysis. *Nucleic Acids Res.* **44**, W160-5.

Rathke, C., Baarends, W. M., Awe, S. and Renkawitz-Pohl, R. (2014). Chromatin dynamics during spermiogenesis. *Biochimica et Biophysica Acta (BBA) - Gene Regulatory Mechanisms* **1839**, 155–168.

Robinson, M. D., McCarthy, D. J. and Smyth, G. K. (2010). edgeR: a Bioconductor package for differential expression analysis of digital gene expression data. *Bioinformatics* **26**, 139–140.

Ryan Corces, M., Trevino, A. E., Hamilton, E. G., Greenside, P. G., Sinnott-Armstrong, N. A., Vesuna, S., Satpathy, A. T., Rubin, A. J., Montine, K. S., Wu, B., et al. (2017). An improved ATAC-seq protocol reduces background and enables interrogation of frozen tissues. *Nat. Methods* **14**, 959–962.

Schindelin, J., Arganda-Carreras, I., Frise, E., Kaynig, V., Longair, M., Pietzsch, T., Preibisch, S., Rueden, C., Saalfeld, S., Schmid, B., et al. (2012). Fiji: an open-source platform for biological-image analysis. *Nat. Methods* **9**, 676–682.

Schultz, R. M. (2002). The molecular foundations of the maternal to zygotic transition in the preimplantation embryo. *Hum. Reprod. Update* **8**, 323–331.

Selokar, N. L., Saini, M., Agrawal, H., Palta, P., Chauhan, M. S., Manik, R. and Singla, S. K. (2016). Buffalo (Bubalus bubalis) SCNT embryos produced from somatic cells isolated from frozen-thawed semen: effect of trichostatin A on the in vitro and in vivo developmental potential, quality and epigenetic status. *Zygote* **24**, 549–553.

Shao, Z., Zhang, Y., Yuan, G.-C., Orkin, S. H. and Waxman, D. J. (2012). MAnorm: a robust model for quantitative comparison of ChIP-Seq data sets. *Genome Biol.* **13**, R16.

Shen, L., Shao, N., Liu, X. and Nestler, E. (2014). ngs.plot: Quick mining and visualization of next-generation sequencing data by integrating genomic databases. *BMC Genomics* **15**, 284.

Siklenka, K., Erkek, S., Godmann, M., Lambrot, R., McGraw, S., Lafleur, C., Cohen, T., Xia, J., Suderman, M., Hallett, M., et al. (2015). Disruption of histone methylation in developing sperm impairs offspring health transgenerationally. *Science* **350**,.

Sin, H.-S., Kartashov, A. V., Hasegawa, K., Barski, A. and Namekawa, S. H. (2015). Poised chromatin and bivalent domains facilitate the mitosis-to-meiosis transition in the male germline. *BMC Biol.* **13**, 53.

Sofikitis, N. V., Miyagawa, I., Agapitos, E., Pasyianos, P., Toda, T., Hellstrom, W. J. and Kawamura, H. (1994). Reproductive capacity of the nucleus of the male gamete after completion of meiosis. *J. Assist. Reprod. Genet.* **11**, 335–341.

Tanaka, A., Nagayoshi, M., Takemoto, Y., Tanaka, I., Kusunoki, H., Watanabe, S., Kuroda, K., Takeda, S., Ito, M. and Yanagimachi, R. (2015). Fourteen babies born after round spermatid injection into human oocytes. *Proc. Natl. Acad. Sci. U. S. A.* **112**, 14629–14634.

Tanaka, A., Suzuki, K., Nagayoshi, M., Tanaka, A., Takemoto, Y., Watanabe, S., Takeda, S., Irahara, M., Kuji, N., Yamagata, Z., et al. (2018). Ninety babies born after round spermatid injection into oocytes: survey of their development from fertilization to 2 years of age. *Fertil. Steril.* **110**, 443–451.

Tatehana, M., Kimura, R., Mochizuki, K., Inada, H. and Osumi, N. (2020). Comprehensive histochemical profiles of histone modification in male germline cells during meiosis and spermiogenesis: Comparison of young and aged testes in mice. *PLoS One* **15**, e0230930.

Tekayev, M. and Vuruskan, A. K. (2021). Clinical values and advances in round spermatid injection (ROSI). *Reprod. Biol.* **21**, 100530.

Teperek, M., Simeone, A., Gaggioli, V., Miyamoto, K., Allen, G. E., Erkek, S., Kwon, T., Marcotte, E. M., Zegerman, P., Bradshaw, C. R., et al. (2016). Sperm is epigenetically programmed to regulate gene transcription in embryos. *Genome Res.* **26**, 1034–1046.

Tesarik, J., Mendoza, C. and Testart, J. (1995). Viable embryos from injection of round spermatids into oocytes. *N. Engl. J. Med.* **333**, 525.

Tesarik, J., Rolet, F., Brami, C., Sedbon, E., Thorel, J., Tibi, C. and Thébault, A. (1996). Spermatid injection into human oocytes. II. Clinical application in the treatment of infertility due to non-obstructive azoospermia. *Hum. Reprod.* **11**, 780–783.

Ueda, J., Harada, A., Urahama, T., Machida, S., Maehara, K., Hada, M., Makino, Y., Nogami, J., Horikoshi, N., Osakabe, A., et al. (2017). Testis-specific histone variant H3t gene is essential for entry into spermatogenesis. *Cell Rep.* **18**, 593–600.

Wang, L., Wang, S. and Li, W. (2012). RSeQC: quality control of RNA-seq experiments. *Bioinformatics* **28**, 2184–2185.

Wang, C., Liu, X., Gao, Y., Yang, L., Li, C., Liu, W., Chen, C., Kou, X., Zhao, Y., Chen, J., et al. (2018). Reprogramming of H3K9me3-dependent heterochromatin during mammalian embryo development. *Nat. Cell Biol.* **20**, 620–631.

Wu, J., Huang, B., Chen, H., Yin, Q., Liu, Y., Xiang, Y., Zhang, B., Liu, B., Wang, Q., Xia, W., et al. (2016). The landscape of accessible chromatin in mammalian preimplantation embryos. *Nature* **534**, 652–657.

Xia, W. and Xie, W. (2020). Rebooting the Epigenomes during Mammalian Early Embryogenesis. *Stem Cell Reports* **15**, 1158–1175.

Yamaguchi, K., Hada, M., Fukuda, Y., Inoue, E., Makino, Y., Katou, Y., Shirahige, K. and Okada, Y. (2018). Re-evaluating the Localization of Sperm-Retained Histones Revealed the Modification-Dependent Accumulation in Specific Genome Regions. *Cell Rep.* **23**, 3920–3932.

Yoshida, K., Muratani, M., Araki, H., Miura, F., Suzuki, T., Dohmae, N., Katou, Y., Shirahige, K., Ito, T. and Ishii, S. (2018). Mapping of histone-binding sites in histone replacement-completed spermatozoa. *Nat. Commun.* **9**, 3885.

Zhang, Y., Liu, T., Meyer, C. A., Eeckhoute, J., Johnson, D. S., Bernstein, B. E., Nusbaum, C., Myers, R. M., Brown, M., Li, W., et al. (2008). Model-based analysis of ChIP-Seq (MACS). *Genome Biol.* **9**, R137.

Zhang, T., Cooper, S. and Brockdorff, N. (2015). The interplay of histone modifications – writers that read. *EMBO Rep.* **16**, 1467–1481.

Zhang, B., Zheng, H., Huang, B., Li, W., Xiang, Y., Peng, X., Ming, J., Wu, X., Zhang, Y., Xu, Q., et al. (2016). Allelic reprogramming of the histone modification H3K4me3 in early mammalian development. *Nature* **537**, 553–557.

Zhang, D., Xie, D., Lin, X., Ma, L., Chen, J., Zhang, D., Wang, Y., Duo, S., Feng, Y., Zheng, C., et al. (2018). The transcription factor SOX30 is a key regulator of mouse spermiogenesis. *Development* **145**,.

Zhao, M., Shirley, C. R., Mounsey, S. and Meistrich, M. L. (2004). Nucleoprotein transitions during spermiogenesis in mice with transition nuclear protein Tnp1 and Tnp2 mutations. *Biol. Reprod.* **71**, 1016–1025.

Figures

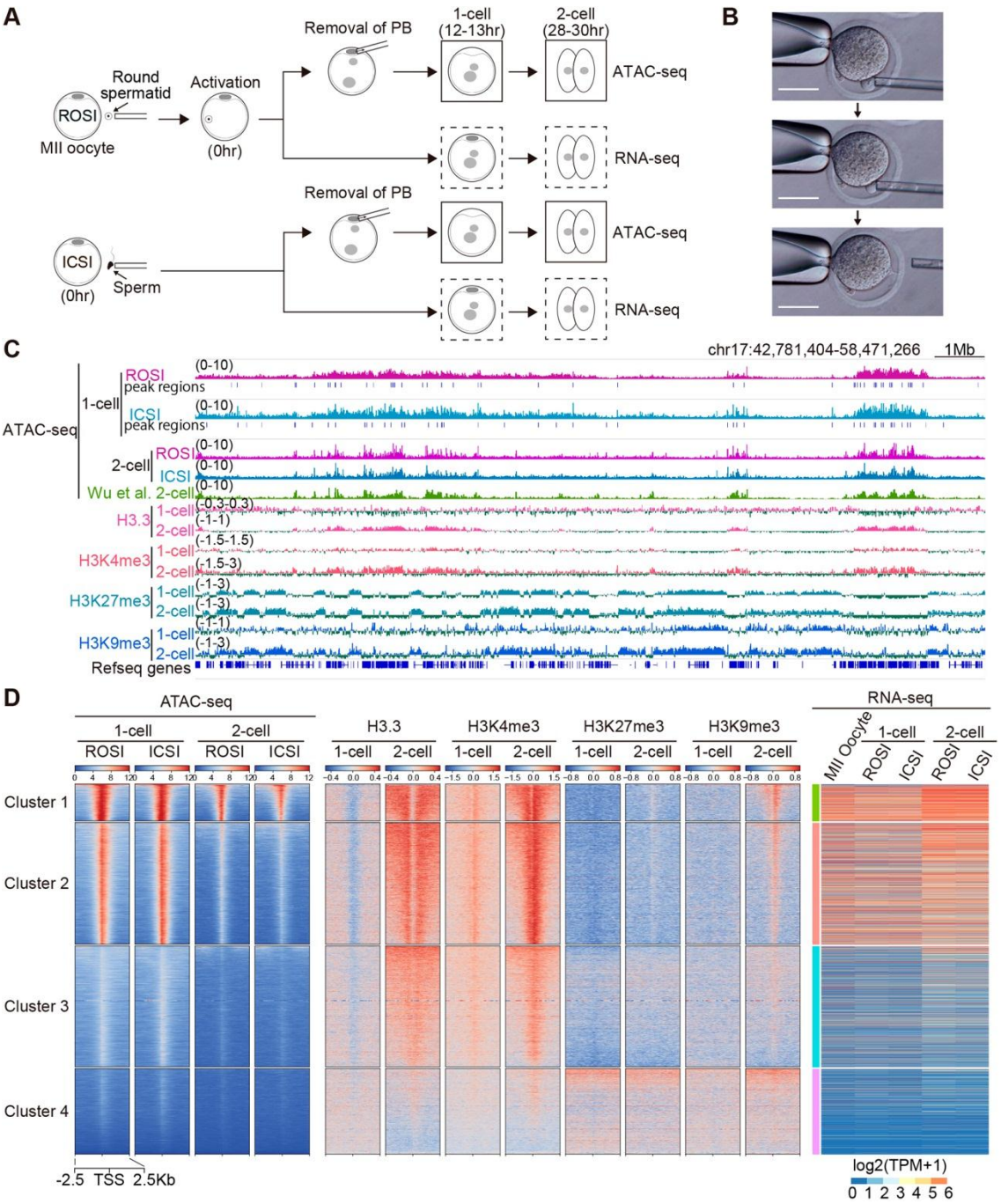

Fig. 1. Chromatin accessibility landscape in ROSI-embryos.

(A) Schematic illustration showing the sample preparation process for chromatin accessibility and transcriptome analyses in ROSI- and ICSI-embryos. The collected samples for ATAC-seq and RNA-seq are indicated by solid and dotted boxes, respectively.

(B) Images showing the process of polar body removal for ATAC-seq. Scale bar, 50 μm.

(C) Genome browser snapshots showing ATAC-seq data and ChIP-seq data for indicated histone modifications or H3.3. ATAC-seq data for 2-cell embryos and ChIP-seq data for H3.3, H3K4me3, H3K27me3, and H3K9me3 for 1-cell and 2-cell data from GSE66390, GSE139527, GSE97778, and GSE73952, respectively (Ishiuchi et al., 2021; Liu et al., 2016; Wang et al., 2018; Wu et al., 2016). ATAC-seq data are shown as reads per kilobase per million reads (RPKM) and ChIP-seq data are shown as log2 ratios between ChIP and input samples.

(D) Left, heatmaps showing normalized ATAC-seq, H3.3, H3K4me3, H3K27me3, and H3K9me3 around TSS (transcription start site) regions. The ATAC signal patterns of 1-cell ROSI, 1-cell ICSI, 2-cell ROSI, and 2-cell ICSI were subjected to k-means clustering and showed clusters of 1-4. Right, expression levels of corresponding genes in M II oocyte (E-MTAB-2950, Abe et al., 2015), ROSI- and ICSI-embryos. Transcriptional levels are indicated by TPM (transcripts per million) (See also Fig.S1F).

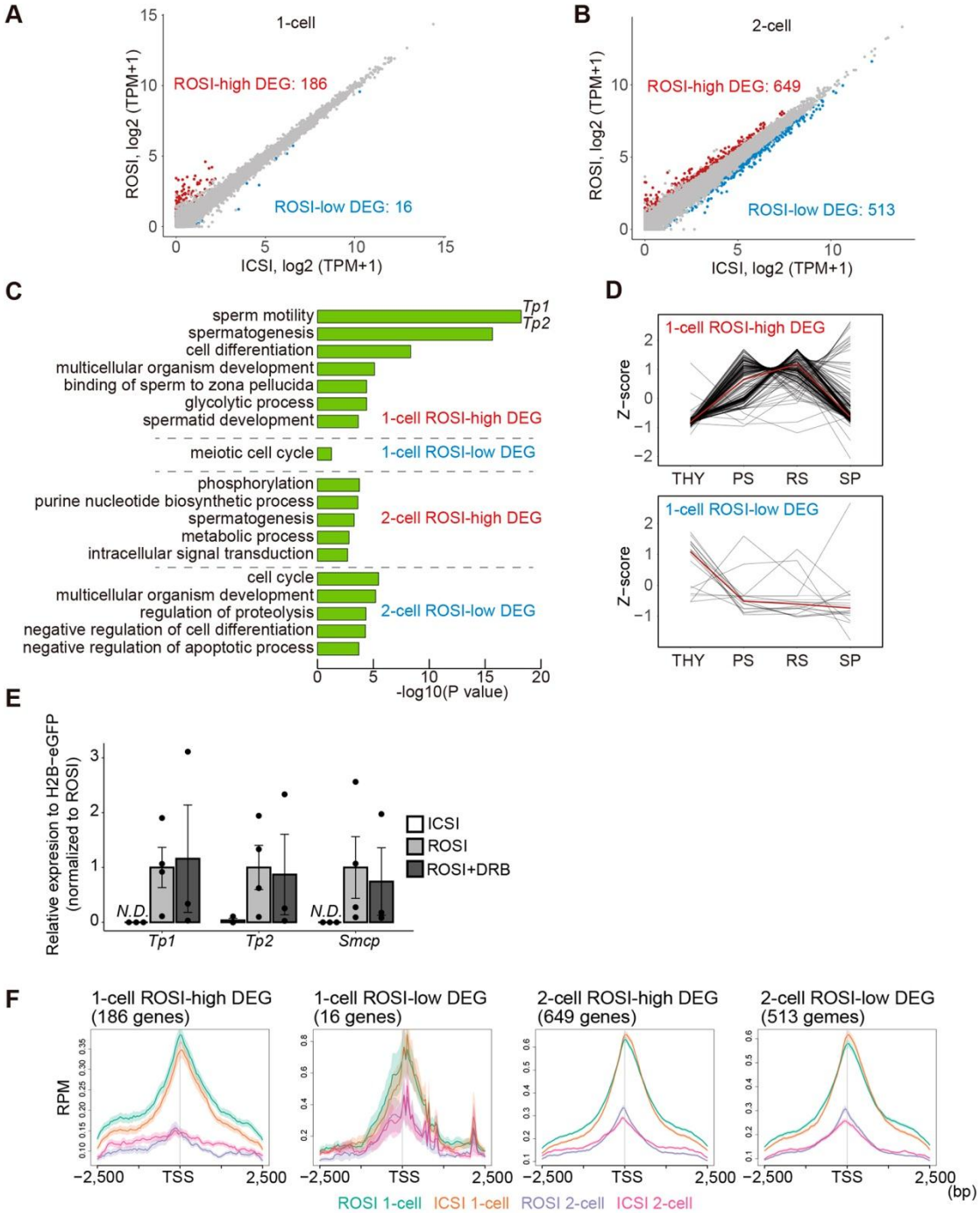

Fig. 2. Differentially expressed genes (DEGs) in ROSI-embryos.

(A and B) Scatter plots comparing gene expression levels between ROSI- and ICSI-embryos at the 1-cell stage (A) or 2-cell stage (B). Upregulated genes (FDR < 0.01 and FC > 1.5, indicated as ROSI-high) and downregulated genes (FDR < 0.01 and FC > 1.5, indicated as ROSI-low) in ROSI-embryos are coloured with red and blue, respectively.

(C) Gene ontology (GO) analysis of the four DEG groups indicated in (A) and (B). Transition protein 1 (Tp1) and Tp2 were included in the term ‘sperm motility’.

(D) Gene expression kinetics of 1-cell DEGs during spermatogenesis. Published RNA-seq data (GSE55060 and DRA000484) (Hasegawa et al., 2015; Kobayashi et al., 2012) were used and shown as Z-scores based on TPM values. THY, undifferentiated spermatogonia; PS, pachytene spermatocytes; RS, round spermatid; SP, sperm.

(E) Quantitative real-time polymerase chain reaction (qRT-PCR) confirmation of RNA transmission from round spermatid. DRB (5,6-dichloro-1-β-D-ribofuranosyl-benzimidazole) inhibits transcription as reported by Abe et al. 2018 (see also Fig. S2A). qRT-PCR analyses of 1-cell ROSI-high genes (*Tp1, Tp2, and Smcp*) in ICSI, ROSI, and DRB-treated ROSI 1-cell embryos (at least three biological replicates). Gene expression was first normalized using the expression of H2B-eGFP as external control and divided by the mean value of ROSI embryos. Data are presented as the mean value. Error bars indicate the standard error of the mean. Dots indicate each data point. Values not detected (N.D.) were represented as 0.

(F) Chromatin accessibility at promoters of each DEG group. Accessibilities of ROSI 1-cell, ICSI 1-cell, ROSI 2-cell, and ICSI 2-cell are colored differently. ATAC-seq data are shown as RPM.

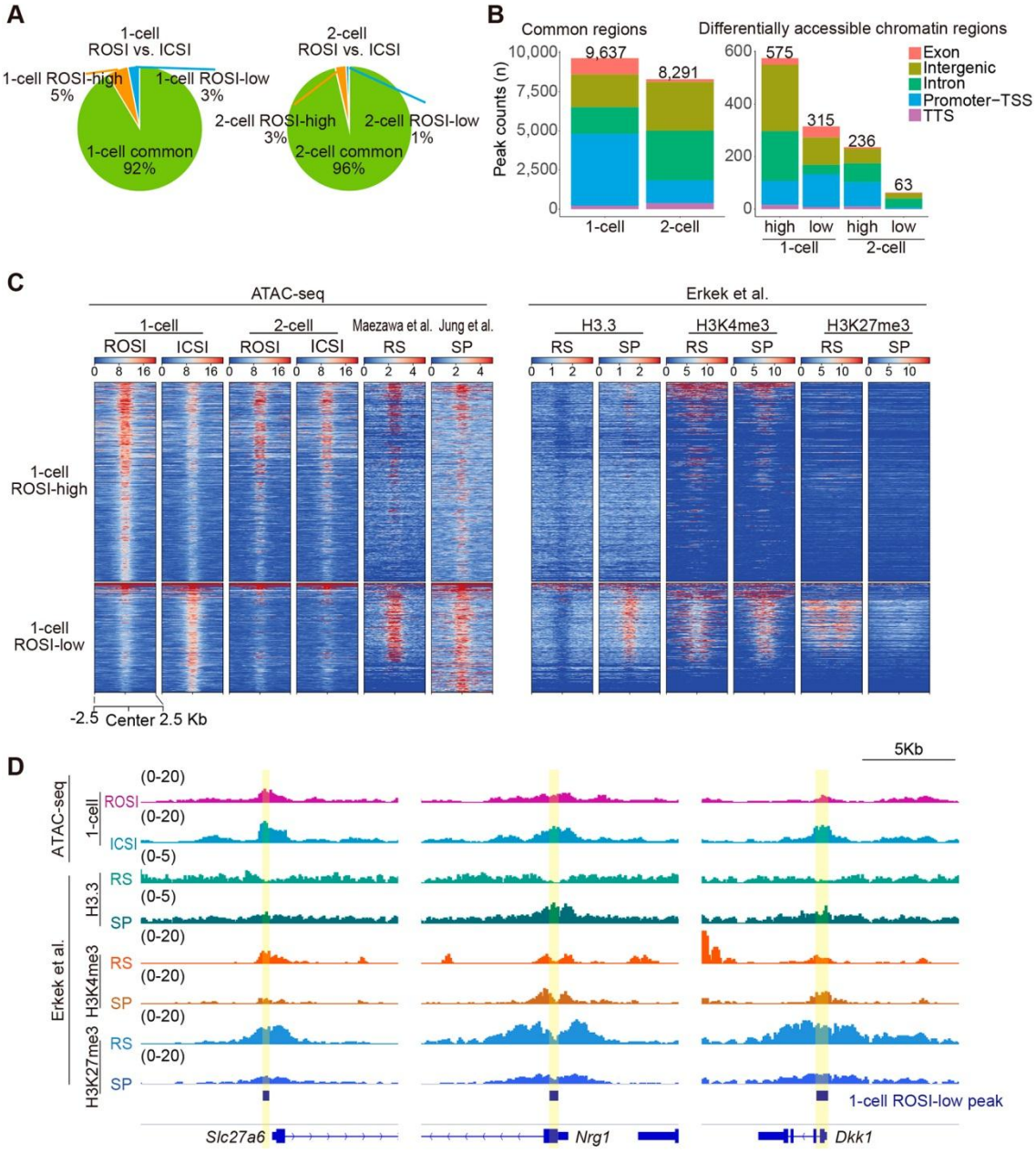

Fig. 3. Differentially accessible chromatin regions in ROSI-embryos indicate signs of epigenetic inheritance from round spermatids.

(A) The fraction of ATAC peaks is classified into common, ROSI-high, or ROSI-low at the 1-cell stage (left) or 2-cell stage (right). Differentially accessible chromatin regions were detected using MACS and MAnorm (see Materials and Methods).

(B) The genomic location of each peak. TTS, transcription termination site.

(C) Heatmaps showing ATAC-seq data (left) and ChIP-seq data for H3.3, H3K4me3, and H3K27me3 in differentially accessible chromatin regions. ATAC-seq and ChIP-seq data for round spermatid (RS) and sperm (SP) were obtained from GSE102954, GSE116857, and GSE42629

(Erkek et al., 2013; Jung et al., 2019; Maezawa et al., 2018a). Heatmaps are shown with RPKM. See also Fig. S4A, B.

(D) Genome browser snapshots showing representative genomic regions with decreased promoter chromatin accessibility in 1-cell ROSI-embryos. 1-cell ROSI-low peak regions are highlighted in light yellow. See also Fig. S5.

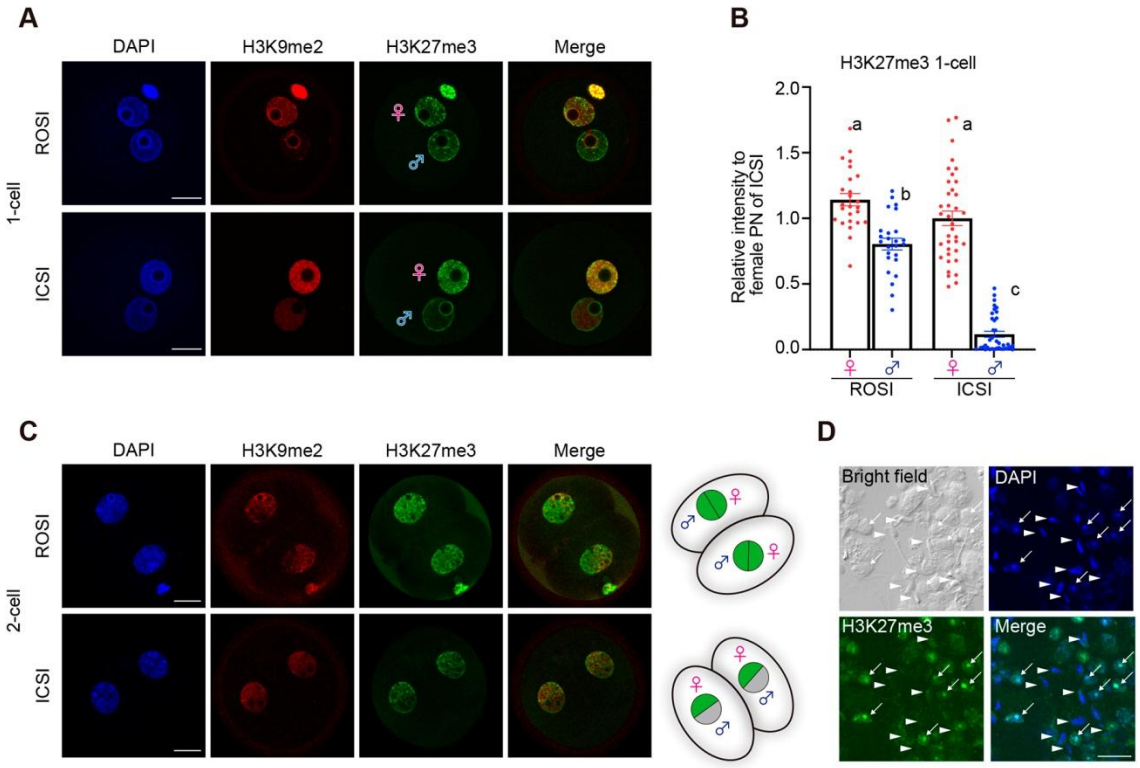

Fig. 4. Immunostaining for H3K27me3 in ROSI- and ICSI-embryos.

(A) Images of immunostaining for H3K27me3 and H3K9me2 in ROSI- and ICSI-embryos at the 1-cell stage. Scale bar, 20 μm.

(B) Plots showing H3K27me3 signal intensity in the female and male PN of 1-cell embryos. Values are normalized by the signal intensity of DAPI (4',6-diamidino-2-phenilindole). Different characters indicate significant differences ($p < 0.05$, by one-way ANOVA and Tukey's multi-comparisons test). Error bars indicate the standard error of the mean. ROSI- and ICSI-embryos were analyzed at n = 37 and n = 25, respectively.

(C) Images of immunostaining for H3K27me3 and H3K9me2 in ROSI- and ICSI-embryos at the 2-cell stage. Scale bar, 20 μm. ROSI- and ICSI-embryos were analyzed n = 31 and n = 28, respectively.

(D) Images of immunostaining for H3K27me3 in spermatogenic cells. Minced seminiferous tubules were subjected to immunostaining. SP and RSs are shown as arrowheads and arrows, respectively. Scale bar, 20 μm.

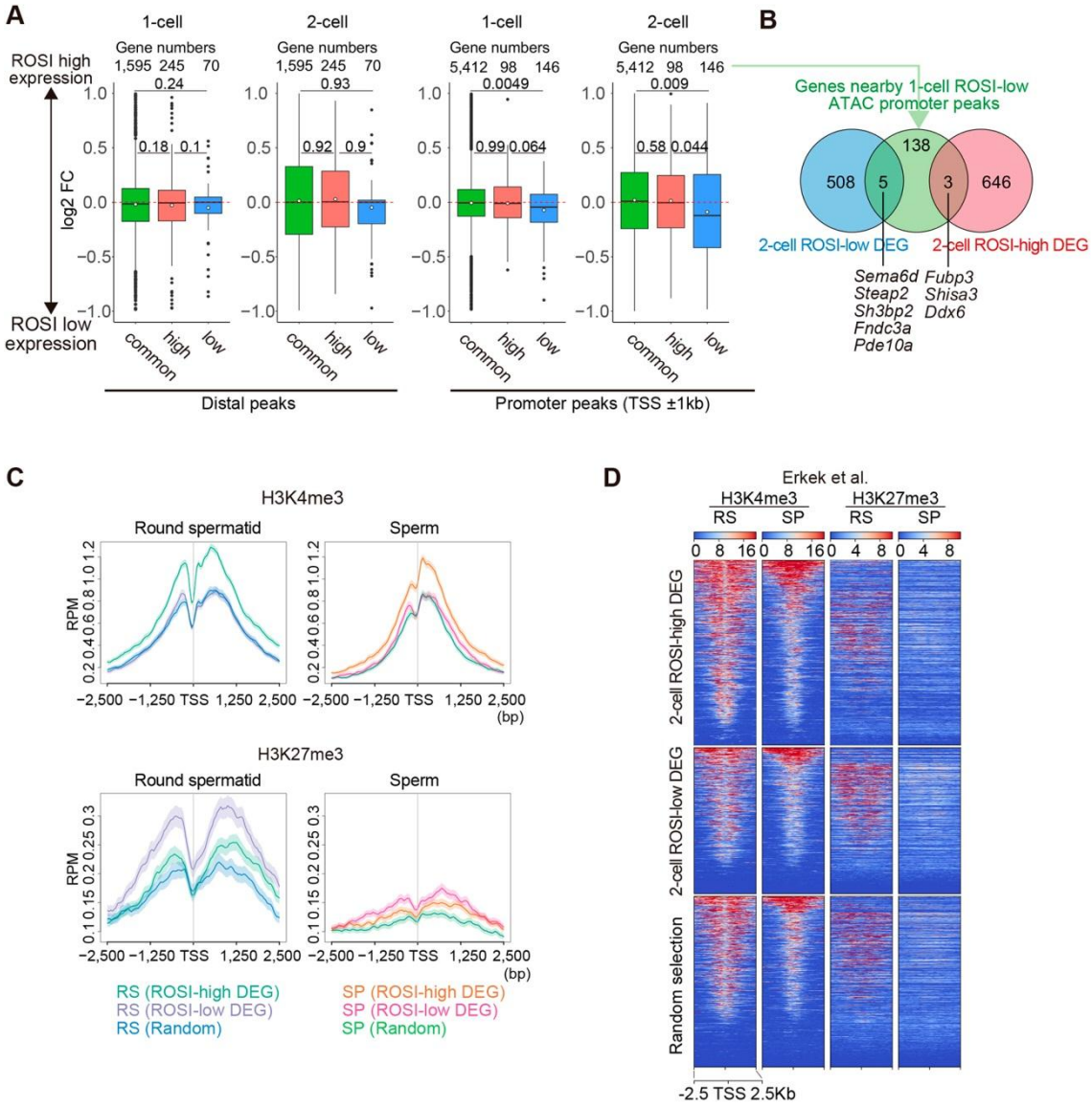

Fig. 5. Altered chromatin accessibility in ROSI-embryos affects gene expression.

(A) Box plots showing differences in gene expression between ROSI- and ICSI-embryos at the 1- or the 2-cell stage. ATAC peak regions were divided into two groups “distal” and “promoter” peaks. Then, the expression was analyzed on the genes associated with the indicated ATAC peak regions defined as “common”, “high”, or “low” accessibility at distal or promoter peaks. Open circles indicate mean values. The number of genes in each group is indicated above the box plots. The p values were calculated using Kruskal–Wallis test.

(B) Venn diagrams showing the overlap between the DEGs in ROSI 2-cell embryos and genes associated with 1-cell ROSI-low promoter ATAC peaks are shown. The overlapping genes are also indicated.

(C and D) Enrichment of H3K4me3 and H3K27me3 in round spermatid (RS) or sperm (SP) around the TSSs of the DEGs in 2-cell ROSI-embryos. Published ChIP-seq data (GSE42629) (Erkek et al., 2013) were used. (C) The enrichment was presented as the average value. H3K4me3 (upper) and H3K27me3 (lower) enrichment in RS (left) and SP (right) around TSS of ROSI-high DEG, ROSI-low DEG, and randomly selected genes are colored differently. ChIP-seq data are shown as RPM. (D) Heatmaps show the enrichment of each DEG group and randomly selected genes as RPKM values.

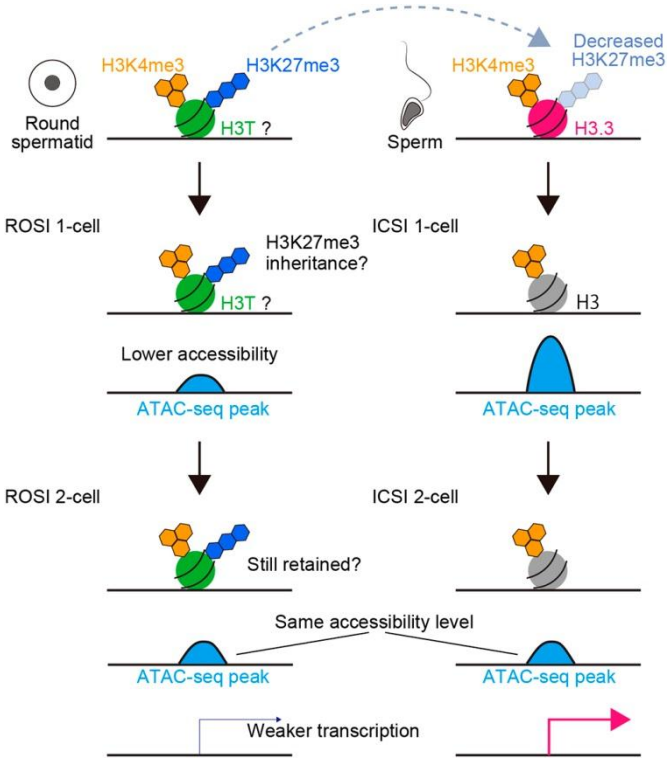

Fig. 6. Model of the effects of epigenetic inheritance from round spermatids on chromatin accessibility and gene expression in ROSI-embryos.

The promoter regions with lower accessible chromatin regions in ROSI-embryos at the 1-cell stage correspond to bivalent chromatin regions marked by H3K4me3 and H3K27me3 in round spermatids (left column). The genes associated with this lower accessibility at the 1-cell stage were more weakly expressed after cleavage to the 2-cell stage though the differential chromatin accessibility was not observed at the 2-cell stage. Note that 1-cell embryos have extremely limited transcriptional activity, and thus it is difficult to detect its alteration using a conventional RNA-seq technique employed in this study. Therefore, currently, we cannot exclude the possibility that embryos at the 1-cell stage may also have some defect in the expression of these genes. Conversely, these regions are marked by high H3K4me3 and decreased H3K27me3 in sperm, are enriched in H3.3, and show higher accessibility in ICSI 1-cell embryos (right column). Therefore, H3K27me3 in round spermatids inherited in ROSI-embryos may suppress gene expression. Since these regions in sperm are enriched in H3.3, H3K27me3 enrichment may be reduced by replacing H3T with H3.3 during spermiogenesis.

Fig. S1

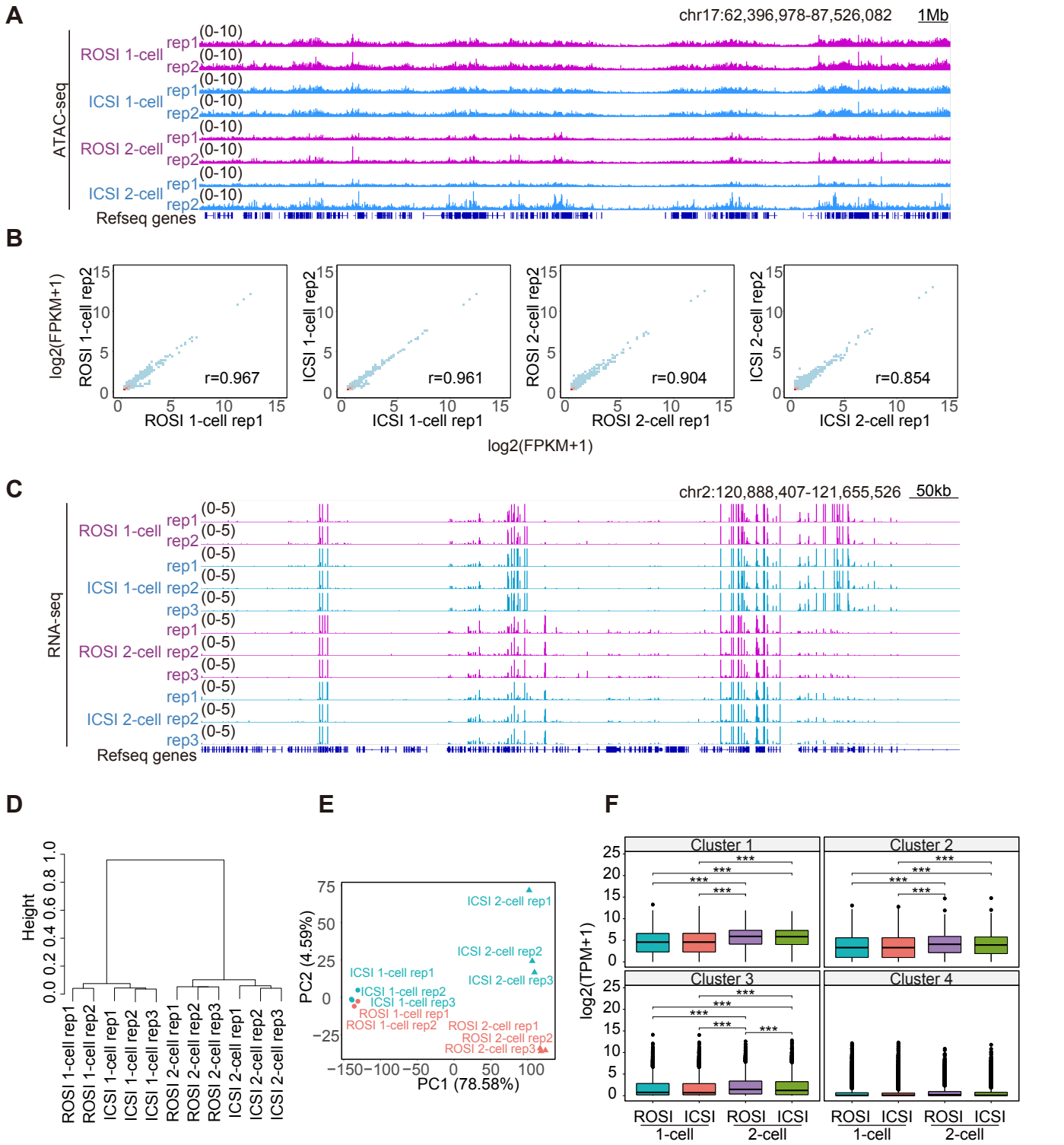

Fig. S1. Validation of ATAC-seq and RNA-seq among replications.
(A) Genome browser snapshots showing ATAC-seq replications. ATAC-seq data are shown as RPKM.
(B) Scatter plots showing ATAC-seq replications. ATAC-seq enrichment was calculated as FPKM (10 kb window for the entire genome). Pearson correlation coefficients are shown.
(C) Genome browser snapshots among RNA-seq replications.
(D) Hierarchical clustering of the global gene expression pattern among RNA-seq replications.
(E) Principal component analysis (PCA) of global gene expression pattern among RNA-seq replications. Red and blue show ROSI and ICSI-embryos, respectively. Circle and triangle symbols show the 1-cell and 2-cell stages, respectively. PCA was calculated log2 (1+TPM) value. The variance of PC1 is 78.58% and PC2 is 4.59%.
(F) Box plots showing expression kinetics among cluster defined by k-means cluster from ATAC-seq TSS signal. ***p < 0.001 and FDR < 0.05, Tukey-Kramer method.

Fig. S2

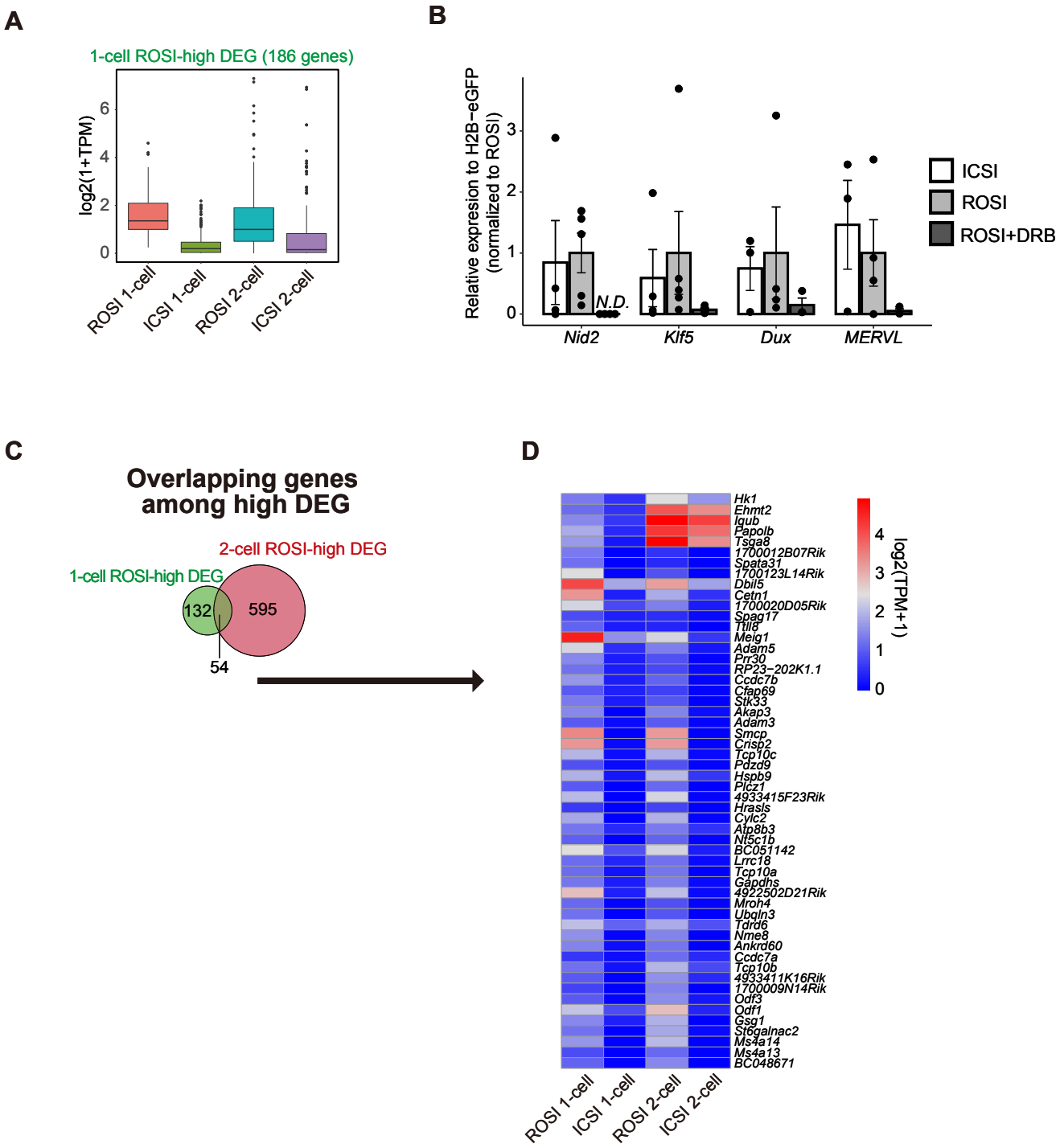

Fig. S2. Features of differentially expressed genes (DEGs) in ROSI-embryos.
(A) Box plots showing expression kinetics of 1-cell ROSI-high DEGs.
(B) DRB (5,6-dichloro-1-β-D-ribofuranosyl-benzimidazole) inhibits transcription as reported by Abe et al., 2018. Quantitative real-time PCR analyses of minor ZGA genes (*Nid2*, *Klf5*, *Dux*, and *MERVL*) and H2B-eGFP as an external control expression in 1-cell ICSI, ROSI, and DRB-treated ROSI-embryos (at least three biological replicates). Gene expression was first normalized using the expression of H2B-eGFP and divided by the mean value of ROSI-embryos. Data are presented as the mean value. Error bars indicate the standard error of the mean. Dots indicate each data point. *Nid2* was not detected in DRB-treated ROSI-embryos.
(C) Overlapping genes between 1-cell ROSI-high-DEG and 2-cell ROSI-high DEG. A total of 54 genes overlapped.
(D) Heatmap showing expression kinetics of overlapped genes of ROSI-high DEG as shown in (C).

Fig. S3

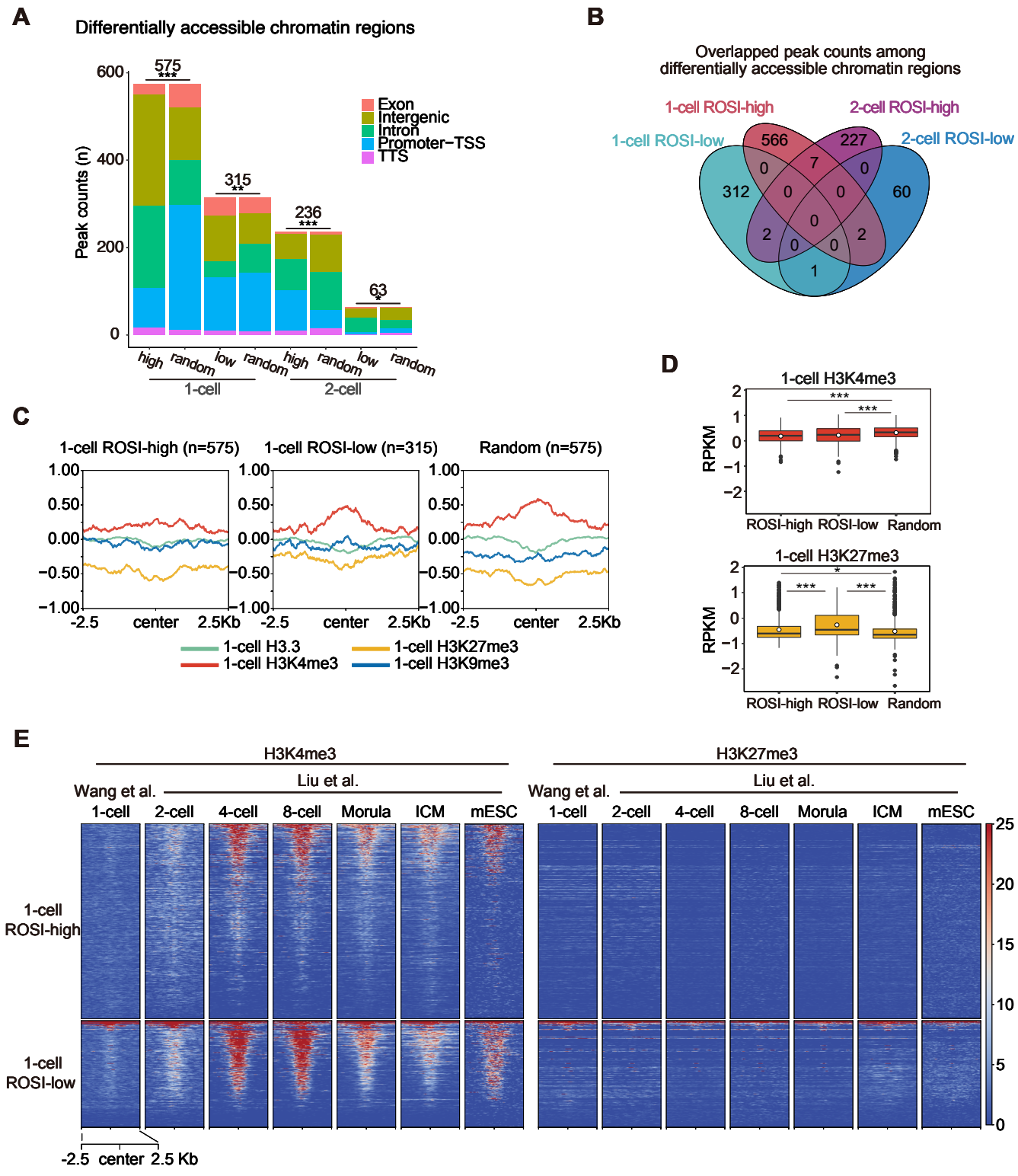

Fig. S3. Features of differentially accessible chromatin regions.
(A) The genomic location of each peak and randomly selected peaks from all the peaks of ROSI 1-cell or 2-cell all peaks. Asterisks indicate significant differences as *p<0.05, **p<0.01, and *** p< 0.001 (Fisher's Exact Test).
(B) Venn diagrams showing the overlap between each group of differentially accessible chromatin regions.
(C) Enrichment of histone modifications and H3.3 at the 1-cell stage around the regions of differentially accessible chromatin regions and randomly selected regions from all the ATAC peaks of ROSI 1-cell. ChIP-seq data for H3.3, H3K4me3, H3K27me3, and H3K9me3 at the 1-cell stage are from GSE139527 and GSE97778 (Ishiuchi et al., 2021; Wang et al., 2018). ChIP-seq data are shown as RPKM for log2 ratios between ChIP and input samples.
(D) Enrichments of H3K4me3 (upper) and H3K27me3 (lower) are represented as box plots. Open circles indicate mean values. Asterisks indicate significant differences as *p<0.05, **p<0.01, and *** p< 0.001 (Tukey-Kramer test).
(E) Heatmaps showing normalized H3K4me3 (left) and H3K27me3 (right) in each stage of pre-implantation embryos and mouse ES cells (mESC) around 1-cell ROSI-high and ROSI-low ATAC peaks. ChIP-seq data for H3K4me3 and H3K27me3 are from GSE97778 and GSE73952 (Liu et al., 2016; Wang et al., 2018). ChIP-seq enrichment is shown as RPKM values.

Fig. S4

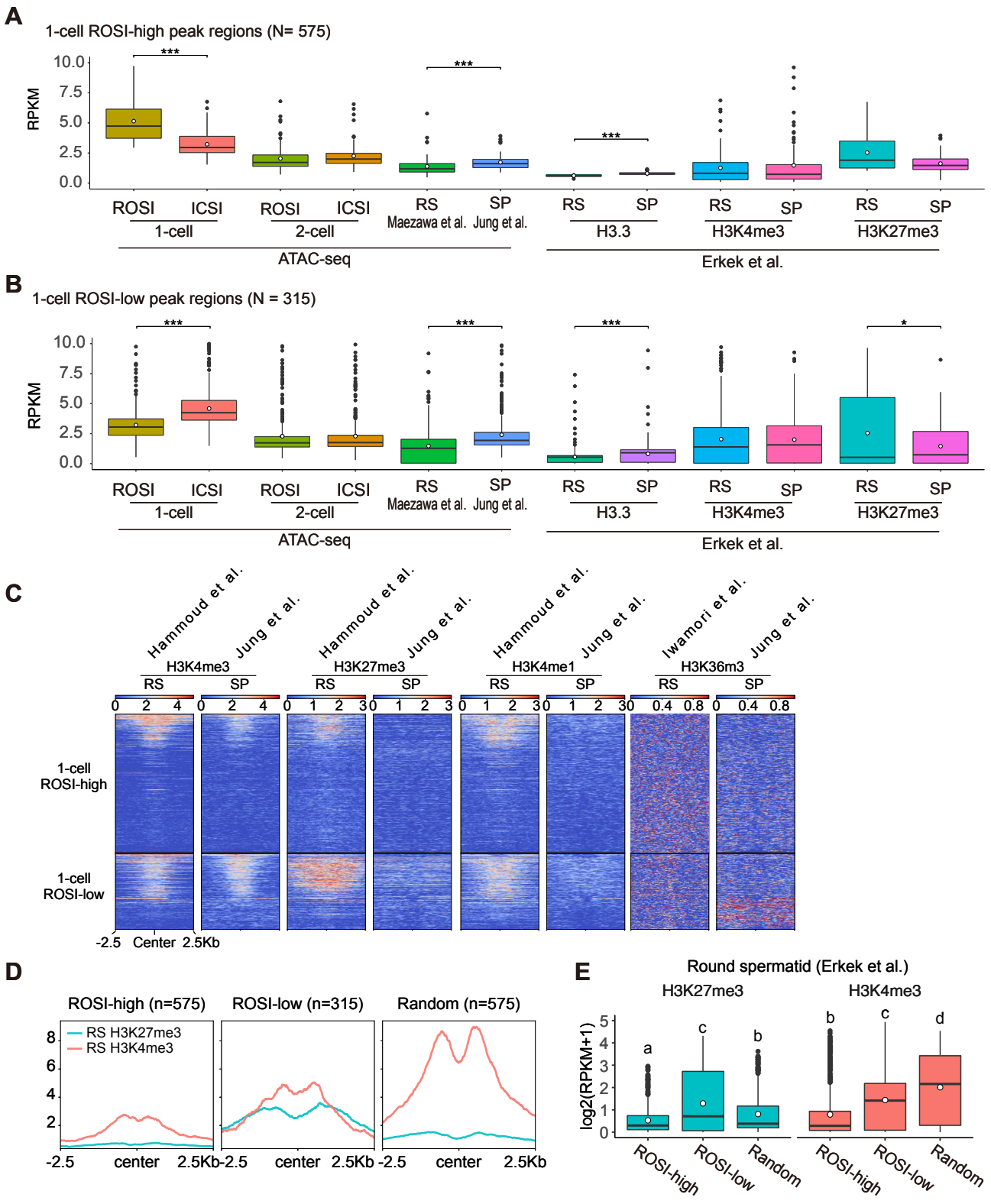

Fig. S4. Characterization of differentially accessible chromatin regions in round spermatids and sperm.
(A and B) Box plots showing ATAC-seq data and ChIP-seq data for H3.3, H3K4me3, and H3K27me3 in differentially accessible chromatin regions. ATAC-seq and ChIP-seq data for round spermatid (RS) and sperm (SP) were obtained from GSE102954, GSE116857, and GSE42629 (Erkek et al., 2013; Jung et al., 2019; Maezawa et al., 2018a). Box plots shown with RPKM in each peak center ± 2,5kb, and open circles are presented as mean values. Asterisks indicate significant differences as *p<0.05, **p<0.01, and *** p< 0.001 (Wilcoxon Rank Sum test). Box plots showing the 1-cell ROSI-high peak regions (A), and 1-cell ROSI-low peak regions (B).
(C) Heatmaps showing ChIP-seq data for H3K4me3, H3K27me3, H3K4me1, and H3K36me3 in differentially accessible chromatin regions. ChIP-seq data for round spermatid (RS) and sperm (SP) were obtained from GSE49624, GSE79230, and DRA004778 (Hammoud et al., 2014; Jung et al., 2017; Iwamori et al., 2016). Heatmaps are shown with RPKM for log2 ratios between ChIP and input samples (H3K4me3, H3K27me3, H3K4me1, and H3K36me3).
(D and E) Enrichment of H3K27me3 and H3K4me3 in round spermatids (Erkek et al., 2013) of differentially accessible chromatin regions and randomly selected regions from ROSI 1-cell all ATAC peaks. (D) The enrichment was shown as the average value around the peak center of each region. (E) The enrichment was represented as box plots. Open circles indicate mean values. Different characters indicate significant differences (Tukey–Kramer test).

Fig. S5

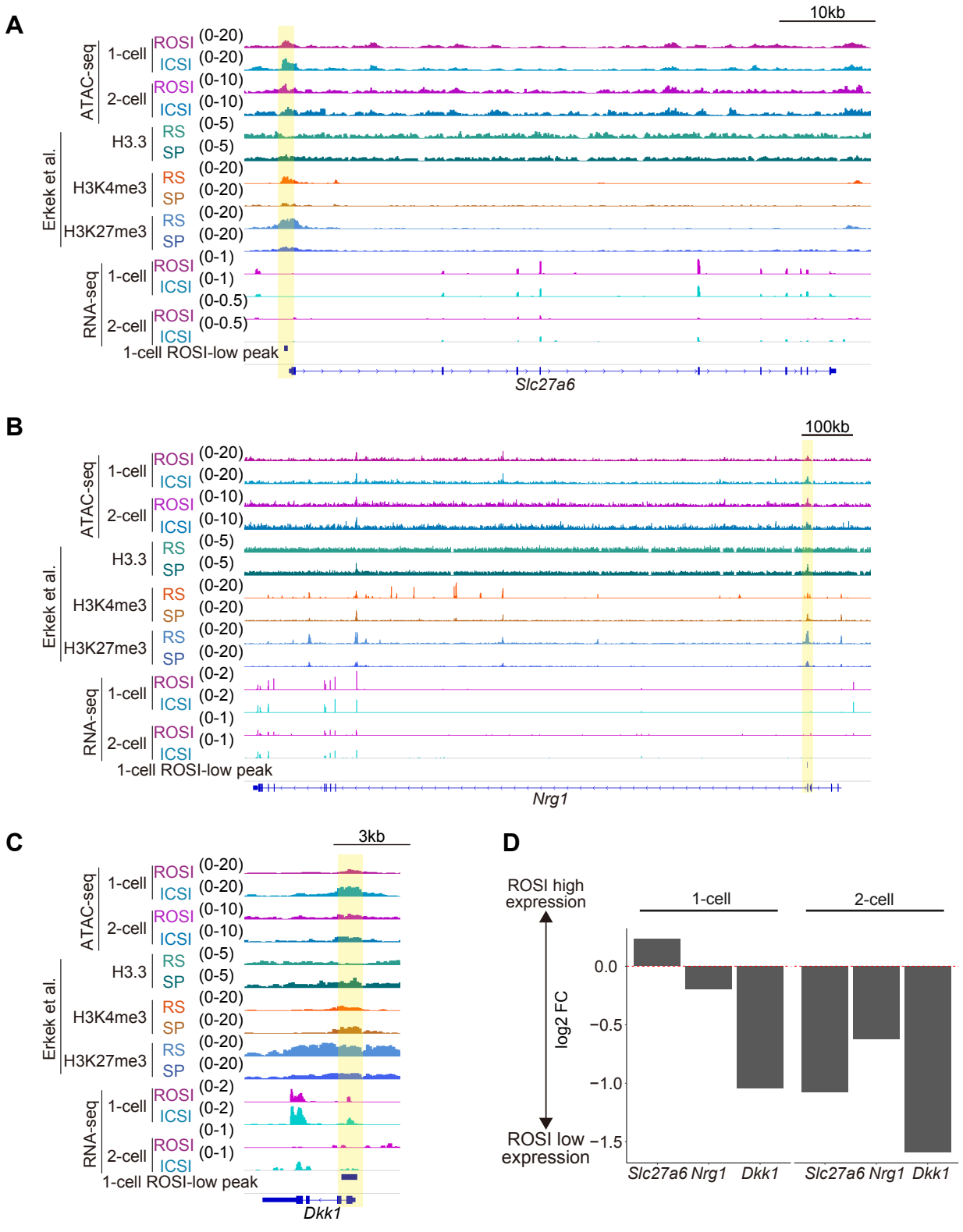

Fig. S5. Genome browser snapshots and gene expression of 1-cell ROSI-low ATAC peak regions.
(A, B, and C) Genome browser snapshots showing representative genes (*Slc27a6* (A), *Nrg1*(B), and *Dkk1*(C)) with decreased promoter chromatin accessibility in 1-cell ROSI-embryos. The 1-cell ROSI-low peak regions are highlighted in light yellow. ChIP-seq data for round spermatid (RS) and sperm (SP) were obtained from GSE42629 (Erkek et al., 2013).
(D) Bar plots showing differences in representative genes between ROSI- and ICSI-embryos at the 1-cell and 2-cell stages.

Fig. S6

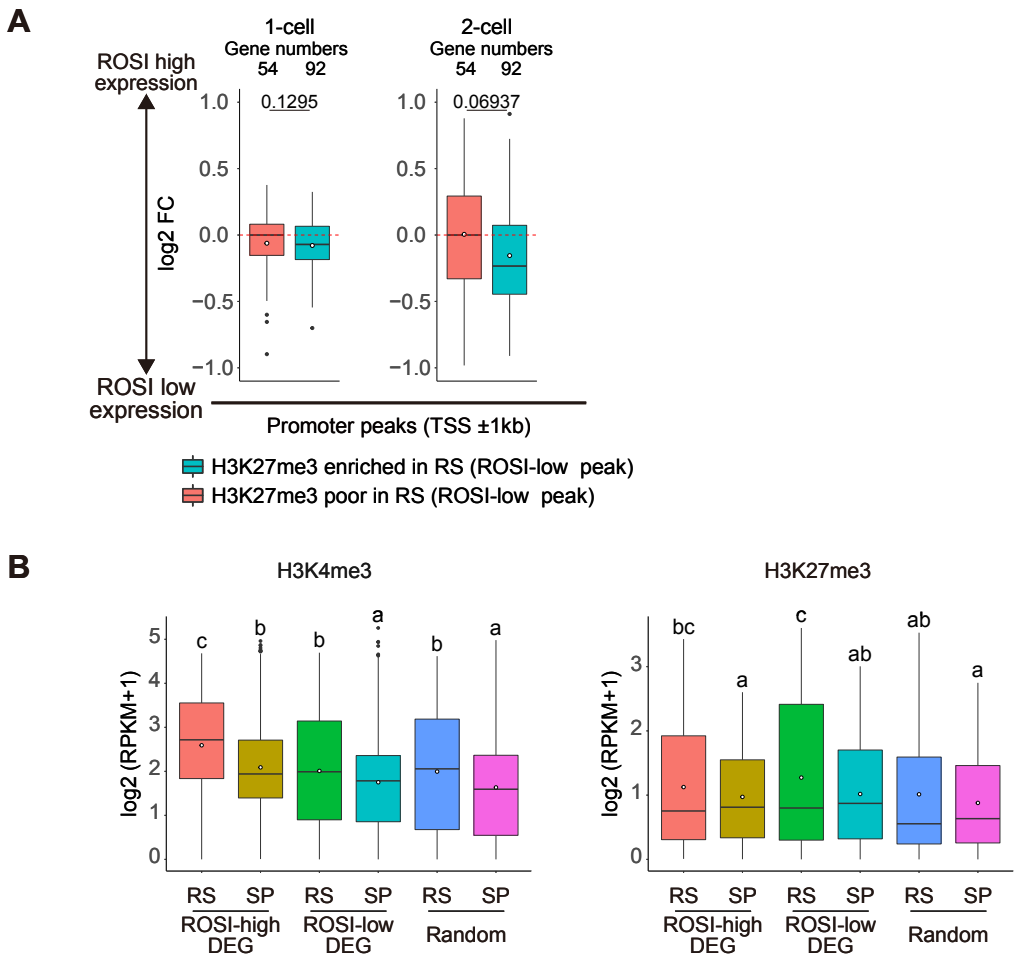

Fig. S6. Altered gene expression in the region with HK27me3 enrichment in round spermatids.
(A) Box plots showing differences in gene expression between ROSI- and ICSI-embryos at the 1- or the 2-cell stages. ATAC promoter peak regions (TSS ± 1kb) within ROSI-low peak regions were divided into two groups “H3K27me3 enriched in RS” (blue) and “H3K27me3 poor in RS” (red) peaks. Then, the expression was analyzed on the genes associated with these ATAC peak regions. Open circles represent the mean values. The number of genes in each group is indicated above the box plots. The p values were calculated using Wilcoxon rank-sum test.
(B) Box plots showing the enrichment of H3K4me3 (left) and H3K27me3 (right) in round spermatid (RS) or sperm (SP) of each DEG group and randomly selected genes as RPKM values. Open circles represent the mean values. Different characters indicate significant differences (Tukey-Kramer test).

Fig. S7

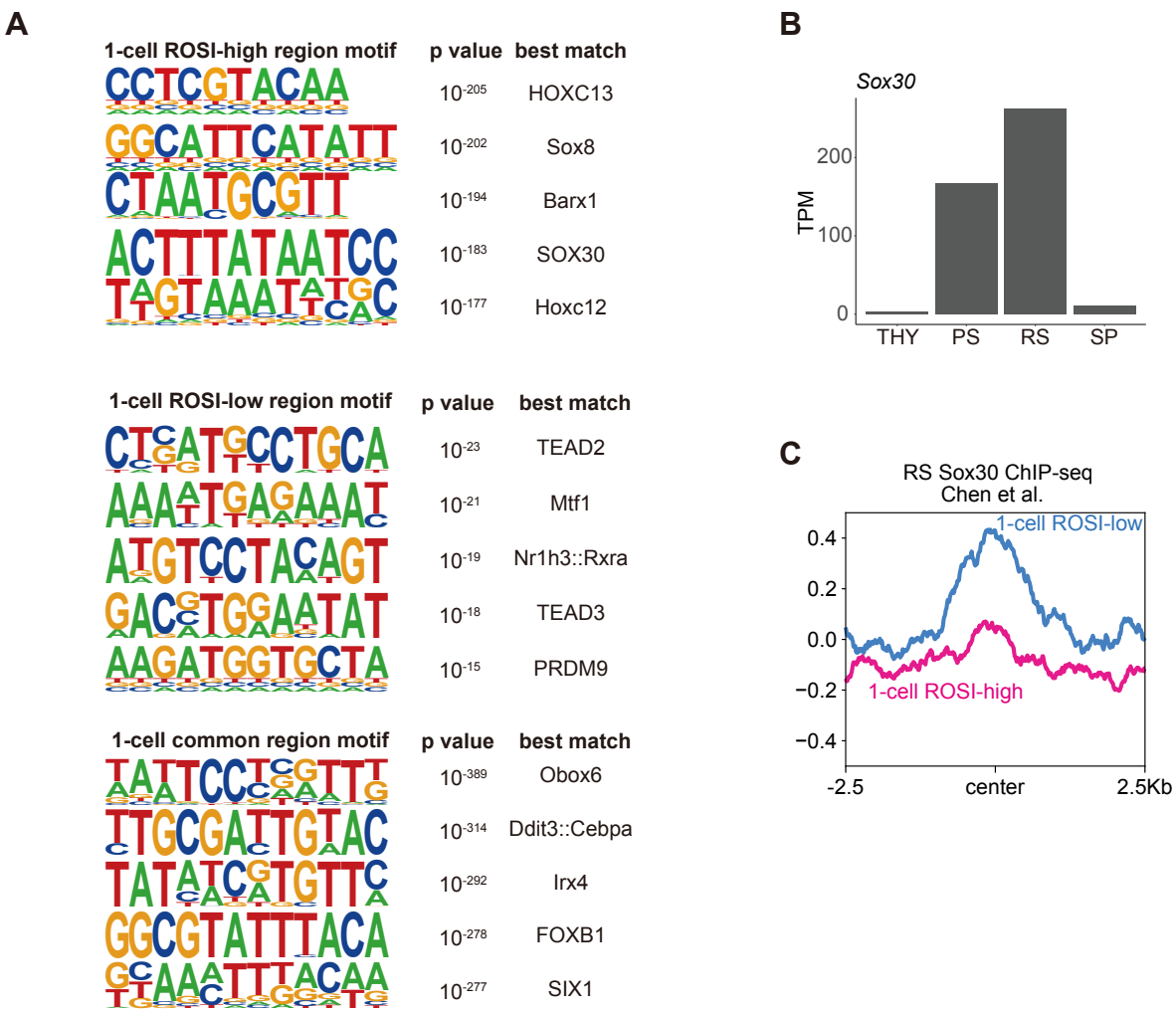

Fig. S7. Motif analysis of 1-cell ROSI high peak regions
(A) Motif analysis of ATAC-peak classified 1-cell ROSI as high, low and common peak for putative transcription factor (TF) binding site was performed using HOMER (Heinz et al., 2010) and the top of five motifs were shown.
(B) Expression value of *Sox30* during representative stages of spermatogenesis; THY undifferentiated spermatogonia; PS pachytene spermatocytes; RS round spermatid; SP sperm. Published RNA-seq data (GSE55060 and DRA000484) (Hasegawa et al., 2015; Kobayashi et al., 2012) were used.
(C) The enrichment of SOX30 in round spermatids using published ChIP-seq data (GSE107644) (Chen et al., 2018b). SOX30 enrichment is shown as RPKM for log2 ratios among input data and colored with pink and blue around 1-cell ROSI-high peak regions and ROSI-low peak regions, respectively.

Table S1.

Click here to download Table S1